ISSN 8755-6839

SCIENCE OF **TSUNAMI HAZARDS**

Journal of Tsunami Society International

Volume 34 **Number 1** **2015**

AN OCEAN DEPTH-CORRECTION METHOD FOR REDUCING MODEL ERRORS IN TSUNAMI TRAVEL TIME: APPLICATION TO THE 2010 CHILE AND 2011 TOHOKU TSUNAMIS **1**

Dailin Wang

NOAA/NWS/Pacific Tsunami Warning Center, 91-270 Fort Weaver Road, Ewa Beach, HI 96706, ***USA****.*
dailin.wang@noaa.gov

THE SPATIAL-TEMPORAL DISTRIBUTIONS OF THE TSUNAMIGENIC EARTHQUAKE SOURCES **23**

Boris Levin[1] & Elena Sasorova[2]

[1]Institute of Marine Geology and Geophysics of RAS, Yuzhno-Sakhalinsk-693022, ***RUSSIA***
[2]Shirshov Institute of Oceanology of RAS, Moscow- 117991, ***RUSSIA***

NUMERICAL SIMULATIONS OF AN EVACUATION FROM A TSUNAMI AT PARANGTRITIS BEACH IN INDONESIA **50**

Radianta Triatmadja - *Department of Civil and Environmental Engineering,*

Tsunami Research Group, Research Centre for Engineering Science
Universitas Gadjah Mada, Yogyakarta, 55281, ***INDONESIA***
radiantatoo@yahoo.com

TSUNAMI SOCIETY INTERNATIONAL, 1741 Ala Moana Blvd. #70, Honolulu, HI 96815, USA.

SCIENCE OF TSUNAMI HAZARDS is a CERTIFIED OPEN ACCESS Journal included in the prestigious international academic journal database DOAJ, maintained by the University of Lund in Sweden with the support of the European Union. SCIENCE OF TSUNAMI HAZARDS is also preserved, archived and disseminated by the National Library, The Hague, NETHERLANDS, the Library of Congress, Washington D.C., USA, the Electronic Library of Los Alamos, National Laboratory, New Mexico, USA, the EBSCO Publishing databases and ELSEVIER Publishing in Amsterdam. The vast dissemination gives the journal additional global exposure and readership in 90% of the academic institutions worldwide, including nation-wide access to databases in more than 70 countries.

OBJECTIVE: Tsunami Society International publishes this interdisciplinary journal to increase and disseminate knowledge about tsunamis and their hazards.

Submit manuscripts of research papers, notes or letters to the Editor. If a research paper is accepted for publication the author(s) must submit a scan-ready manuscript, a Doc, TeX or a PDF file in the journal format. Issues of the journal are published electronically in PDF format. There is a minimal publication fee for authors who are members of Tsunami Society International for three years and slightly higher for non-members. Tsunami Society International members are notified by e-mail when a new issue is available. Permission to use figures, tables and brief excerpts from this journal in scientific and educational works is granted provided that the source is acknowledged.

Recent and all past journal issues are available at: http://www.TsunamiSociety.org CD-ROMs of past volumes may be purchased by contacting Tsunami Society International at postmaster@tsunamisociety.org Issues of the journal from 1982 thru 2005 are also available in PDF format at the U.S. Los Alamos National Laboratory Library http://epubs.lanl.gov/tsunami/

ISSN 8755-6839

SCIENCE OF **TSUNAMI HAZARDS**

Journal of Tsunami Society International

Volume 34 **Number 1** **2015**

AN OCEAN DEPTH-CORRECTION METHOD FOR REDUCING MODEL ERRORS IN TSUNAMI TRAVEL TIME: APPLICATION TO THE 2010 CHILE AND 2011 TOHOKU TSUNAMIS

Dailin Wang
NOAA/NWS/Pacific Tsunami Warning Center, 91-270 Fort Weaver Road, Ewa Beach, HI 96706, USA.
dailin.wang@noaa.gov

ABSTRACT

In this paper, we attempt to reduce the discrepancies between the modeled and observed tsunami arrival times. We treat the ocean as a homogenous fluid, ignoring stratification due to compressibility and variations of temperature and salinity. The phase speed of surface gravity waves is reduced for a compressible fluid compared to that of an incompressible fluid. At the shallow water limit, the reduction in speed is about 0.86% at a water depth of 4000 m. We propose a simple ocean depth-correction method to implement the reduction in wave speed in the framework of shallow water equations of an incompressible fluid: 1) we define an effective ocean depth such that the reduction of the phase speed due to compressibility of seawater is exactly matched by the decrease in water depth (about 2.5% reduction at ocean depth of 6000 m and less than 0.1% at 200 m); 2) this effective depth is treated as if it were the real ocean depth. Implementation of the method only requires replacing the ocean bathymetry with the effective bathymetry so there is no need to modify existing tsunami codes and thus there is no additional computational cost. We interpret the depth-correction method as a bulk-parameterization of the combined effects of physical dispersion, compressibility, stratification, and elasticity of the earth on wave speed. We applied this method to the 2010 Chile and 2011 Tohoku basin-crossing tsunamis. For the 2010 Chile tsunami, this approach resulted in very good agreement between the observed and modeled tsunami arrival times. For the 2011 Tohoku tsunami, we found good agreements between the modeled and the observed tsunami arrival times for most of the DARTs except the farthest ones from the source region, where discrepancies as much as 3-4 min. still remain.

Keywords: *tsunami, numerical modeling, shallow water equations, tsunami travel time*

1. INTRODUCTION

The destructive February 27, 2010 Chile and March 11, 2011 Tohoku basin-crossing tsunamis were recorded at many ocean bottom pressure sensors, the so-called DART buoys. These tsunamis are generally modeled well by researchers (e.g., Saito et al, 2011; Yamazaki and Cheung 2011; Yamazaki et al. 2012; Grilli et al, 2012). The modeled tsunami arrival times however, are generally too early than the observed at the DARTs by as much as 15 minutes. For the 2010 Chile tsunami, Kato et al. (2011) found that tsunami arrival times at GPS buoys near Japan were as much as 26 minutes later than model predictions.

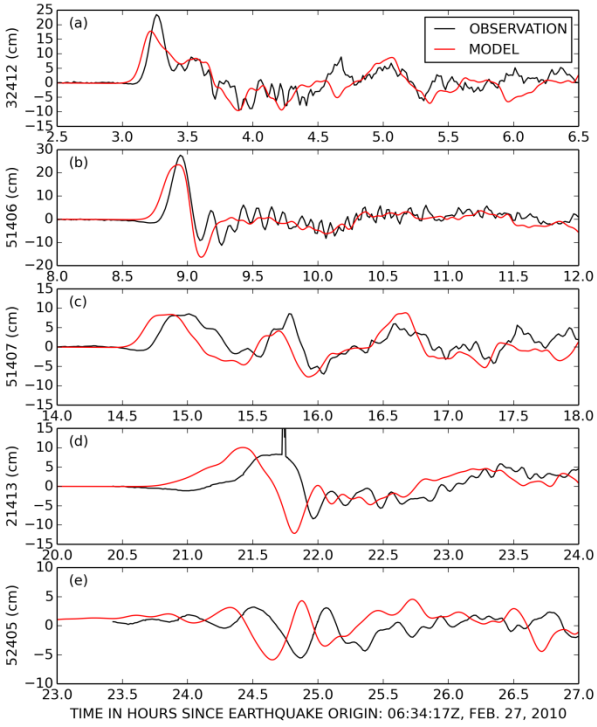

Figure 1. Comparison of RIFT model result with observations at DARTs for the Feb. 27, 2010 Chile tsunami. The model is forced with a rectangular fault with a uniform slip (Mw=8.8). This is a post-event rerun extending integration length from 24 to 30 hours. See Section 3.2 for details of the forcing parameters used. The depth-correction method proposed in this study was not applied to this model run.

For the Chile 2010 tsunami, using the real-time tsunami forecast model RIFT (Wang et al., 2009, Wang et al. 2012), the Pacific Tsunami Warning Center (PTWC) was able to predict the wave propagation across the Pacific basin before the nearest DART recorded the tsunami (Foster et al., 2012, supplemental materials). However, the modeled tsunami arrival times were early compared to the observed ones. The discrepancies increased as the distance from the epicenter increased (Figure 1). For DART 21413 near Japan, for example, the predicted arrival time was about 12 minutes earlier

than the observed (Figure 1d). For DART 52405 near Guam, the modeled and observed tsunami waveforms were completely out of phase (Fig. 1e), after 24 hours of propagation.

For the 2011 Tohoku tsunami, Grilli et al. (2012) noted that the modeled tsunami arrival times were earlier than the observed by as much as 15 minutes. Yamazaki et al. (2012) had similar findings. Figure 2 compares the modeled and observed tsunami waveforms at selected DARTs across the Pacific basin. The model result was obtained by forcing the PTWC RIFT model with the USGS finite fault solution (more details are given in section 3.3). Similar to the 2010 Chile tsunami, the differences between modeled and observed tsunami arrival times increased as the distance to the epicenter increased. Seven hours after the earthquake origin, the tsunami arrived at DART 51407 (near Hawaii) about 8 minutes later than predicted (Figure 2b). After 13 hours of propagation, the tsunami arrived at DART 51406 (near Marquesas Islands) about 12 min. later than predicted (Figure 2c). After 20 hours of propagation, the tsunami arrived at DART 32401 (near Chile) about 17 min. later than predicted, with the second peak from the model lining up with the first observed peak (Figure 2e).

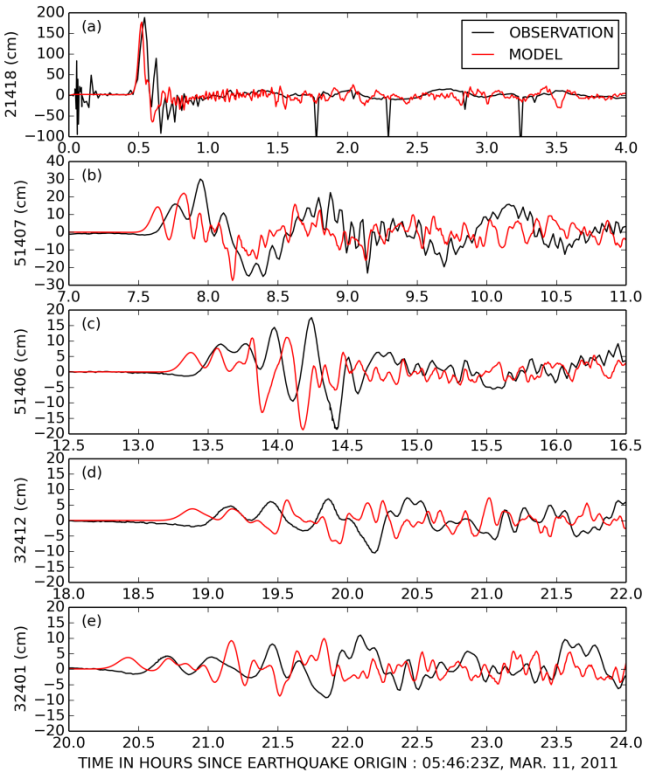

Figure 2. Comparison of RIFT model result without depth-correction with observations at DARTs for the Mar. 11, 2011 Tohoku Tsunami. The model is forced with the USGS finite fault solution (Mw=9.0). See Section 3.3 for details of forcing parameters used.

Surface gravity wave phase speed is known to be reduced for a compressible fluid (e.g., Ward 1980, Okal 1982; Yamamoto 1982) and for compressible fluid with background stratification (Shchepetkin and McWilliams 2011). To accurately model the tides, it is known that effects of ocean self-attraction and loading must be included (e.g., Ray 1998). There have been some efforts in trying to explain the discrepancies of the modeled and observed tsunami arrival times (Watada et al. 2011, Tsai et al 2013; Watada 2013). Tsai et al. (2013) found that the total reduction in phase speed is about 1% at 300 km wavelength for an ocean depth of 4000 m, about 0.55% due to density variation of seawater caused by compressibility and dispersion, and 0.45% due to the elasticity of the earth. At 1000 km wavelength, the total reduction in speed is about 1.5%, about 0.5% due to density variation, and 1.0% due to elasticity of the earth (the larger the wavelength, the greater the effect of earth's elasticity has on wave speed). We note that 1000 km wavelength (or 84 min. period at 4000 m water depth) is not a typical characteristic of a damaging tsunami, although spectral analysis might reveal that wavelengths longer than 1000 km contain some energy. It is difficult however, to separate tidal energy and energy due to very long waves of the tsunamis.

Inazu and Saito (2013) introduced a simple parameterization in the shallow water equations to account for the effect of pressure loading on tsunami propagation, using the method of Ray (1998). This is achieved by introducing a small empirical correction (proportional to the surface height) in the pressure gradient term of the momentum equations, in effect reducing the phase speed of the wave propagation. It is shown that the modeled tsunami arrival times agree much better with those of the observed during the 2010 Chile and 2011 Tohoku tsunamis, with an appropriate choice of the empirical parameter related to the correction term. Their method is computationally efficient and can be easily adopted in existing tsunami codes with minimal modification. However, as in the case of tides (Ray 1998), the optimal value of the empirical parameter varies somewhat for different DARTs to achieve the best fit.

Incorporating the effects of density stratification as well as pressure loading, Allgeyer and Cummins (2014) showed that the discrepancies between the modeled and observed tsunami wave times could be drastically reduced. They were also able to reproduce the initial small depression of the leading wave as observed (not present in classical shallow water results). They derived a surface height equation assuming linear density stratification. The resulting equation contains the average density and ocean bottom density, both varying with the depth of the ocean, assuming a linear density profile. The seafloor deformation due to pressure loading is computed using a Green's function approach. Although their method is self-contained and can be used in tsunami forecasting, it is computationally costly, with the computation of the seafloor deformation accounting for 70% of the total model computation time. Watada et al. (2014, also refer to this reference for a more exhaustive discussion of literature on the subject) applied a phase-correction method to solutions of shallow water equations and were able to significantly reduce the tsunami travel time errors at the DARTs and were also able reproduce the small initial depression of the observed tsunamis as well. It is impractical however, to apply their method to the whole computational domain in a nonlinear forward model.

In this study, we attempt to reduce the discrepancies between modeled and observed tsunami arrival times by adopting a simpler approach, starting with the effect of compressibility. We treat the ocean

as a compressible homogenous fluid. The background stratification due to compressibility is ignored (or Boussinesq fluid). The surface gravity wave speed is reduced in such a system (Yamamoto, 1982).

We propose a simple method to implement this new dispersion relation in a shallow water tsunami forecast model, by defining an effective/equivalent ocean depth/bathymetry in a manner that the reduction in phase speed due to compressibility of seawater is exactly matched by the reduction in water depth. The effective ocean depth differs from the true ocean depth by about 2.5% at 6000 m water depth. At water depth less than 200 m, the difference is negligible (less than 0.1%). Implementation of this method is straightforward and there is no need to modify the numerical codes of tsunami forecast models, thus there is no additional computational cost. All that is needed is to replace the real ocean bathymetry with the effective ocean bathymetry, which can be computed once and for all. We call this approach the ocean depth-correction method. We applied this method to the 2010 Chile and 2011 Tohoku tsunamis. The source models used are purely seismic, without any knowledge of the observed tsunami information. With the depth-correction method, we show that the discrepancies between the modeled and the observed tsunami arrival times are greatly reduced.

2. Surface gravity wave dispersion relation and method of depth-correction

It is well known that compressibility of seawater reduces the phase speed of surface gravity waves (e.g., Ward 1980; Okal 1982). Here, we start with the dispersion relation of wave motions of a compressible homogenous fluid with a free surface (Yamamoto, 1982):

$$\frac{\omega^2}{k'^2} = \frac{g}{k'}\tanh(k'H), \tag{1}$$

where $$k'^2 = k^2 - \frac{\omega^2}{s^2}, \tag{2}$$

k is the wave number, ω the frequency, and s the speed of sound in seawater, assumed to be a constant, 1500 m/s.

In the shallow water limit ($k'H \ll 1$), (1) becomes

$$\frac{\omega^2}{k'^2} = gH. \tag{3}$$

Or in terms of the wave number k,

. $$\frac{\omega^2}{k^2} = gH/(1 + \frac{gH}{s^2}) \tag{4}$$

The dispersion relation (4) is similar to the dispersion relation of classic shallow water surface gravity waves, except it now acquires a factor related to the water depth and sound speed.

We define an effective ocean depth as

$$H_E = H/(1 + \frac{gH}{s^2}) \tag{5}$$

The dispersion relation (4) becomes

$$\frac{\omega^2}{k^2} = gH_E \tag{6}$$

Or the phase speed is

$$C_E = \frac{\omega}{k} = \sqrt{gH_E}. \tag{7}$$

This has the exact form of the classic shallow water wave dispersion relation except the ocean depth is now replaced by an "effective" depth (5). We note that the waves are non-dispersive at the shallow water limit and the phase speed (7) is smaller than the classic shallow water wave speed because $\sqrt{\frac{H_E}{H}} < 1$,

$$C_E = C\sqrt{\frac{H_E}{H}} = C\left(1 - \frac{gH}{2s^2} + \cdots\right), \text{ where } C = \sqrt{gH}, \tag{8}$$

C is the classical shallow water wave phase speed. The second equal sign represents Taylor expansion, for the sake of discussion to follow.

Next we examine the difference between the ocean depth and the effective ocean depth. Figure 3a shows the difference ($H_E - H$) versus the ocean depth *H*. At *H*=6000 m, the difference is 152 m, or 2.5%. At *H*=1000 m, the difference is 4.3 m, or 0.4%. At *H*=200 m, the difference is 0.17 m, or less than 0.1%. We note that global ocean bathymetry datasets are usually only accurate to about 1 m. So we can consider differences of order 1 m negligible as far as accuracy of ocean bathymetry for the open ocean is concerned.

Figure 3b shows the percentage difference between the surface gravity wave phase speed C_E of a compressible ocean with the wave phase speed of incompressible ocean *C*. At 6000 m depth, the phase speed reduction due to compressibility is 1.28%. At 4000 m depth, the reduction is 0.86%. At 1000 m, the reduction is 0.22%. Assuming a tsunami wave crosses the Pacific basin in 24 hours at an average ocean depth of 4000 m, the delay of tsunami arrival time will be about 12 minutes.

In Inanzu and Saito (2013), the dispersion relation is

$$C_E = \sqrt{gH(1-\beta)} = C\left(1 - \frac{\beta}{2} + \cdots\right), \tag{9}$$

Where β is tunable parameter and is independent of the water depth. They found that $\beta = 0.02$, which amounts to 1% correction in phase speed, gave the best result overall. They did show that different values of β are needed to obtain the best fit for different DARTs.

We should point out that dispersion relation (4) neglects the effect of background stratification due to compressibility. When this effect is taken into account (i.e., for a non-Boussinesq fluid), the dispersion relation will be (to leading order of Taylor expansion):

$$C_E = C(1 - \frac{gH}{4s^2}), \tag{10}$$

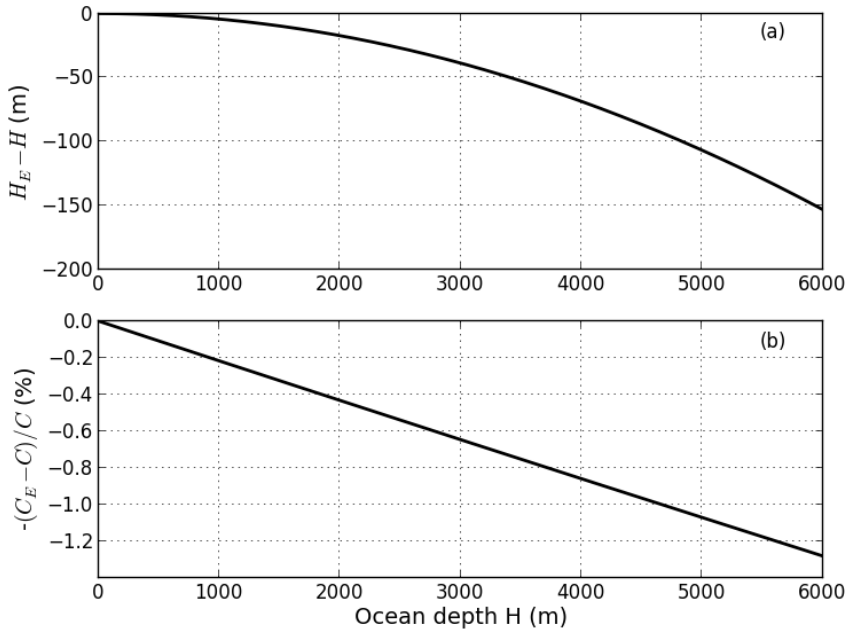

Figure 3. (a) Difference between effective ocean depth defined by equation (5) and true ocean depth; (b) difference between phase speeds of compressible fluid and incompressible fluid, see equation (8).

as derived by Shchepetkin and McWilliams (2011). On the surface, the correction term in equation (4) or equation (8) is off by a factor of two, suggesting (10) should be used. In reality however, the tsunami waves (typical wavelengths of 100-700 km) are weakly dispersive, the shallow water limit is only an approximation. Dispersion alone reduces the wave speed. For example, for a 200 km wavelength at 4000 m depth, the reduction of phase speed is 0.26%. In other words, if a finite wave

number is considered, the difference between (4) and a dispersive version of (10) (see Watada 2013) is not as large as it appears to be for typical tsunami waves. For example, for a 15-min. period wave at 4000 m ocean (180 km wavelength), the phase speed reduction from (4) and from Watada (2013, equation 25) is 0.86% and 0.76% respectively. Only for waves with periods longer than 60 min., does the difference between (4) and that of Watada (2013) approaches to a factor of two.

In light of the fact that elasticity of the earth also reduces the phase speed, we adopt dispersion relation (4) as a "bulk" parameterization, mimicking the combined effects of physical dispersion, compressibility, density variation, and elasticity of the earth on tsunami speed. We call this the depth-correction method. In essence, our approach is similar to the approach of Inazu and Saito (2013) except that our depth correction coefficient is a function of depth and there are no tunable parameters in our approach. In shallow waters the correction is negligible, rather than being a constant fraction everywhere. Implementation of the method is straightforward. All that is needed is to replace the ocean bathymetry with the effective bathymetry (5), thus there is no need to modify existing numerical codes.

3. Application to the 2010 Chile and 2011 Tohoku tsunamis

3.1 The tsunami forecast model and data analysis

We employ the PTWC real-time linear tsunami forecast model RIFT for this study (Wang et al., 2009; Foster et al., 2012; Wang et al., 2012). The RIFT model solves the linear shallow water equations in spherical coordinates with leap-frog stepping in time and centered difference in space (Arakawa and Lamb, 1977), similar to the linear versions of the tsunami model of Kono et al. (2002) and the real-time tsunami forecast model of Yasuda et al (2013). For bathymetry, we use the GEBCO 30-arc-sec data [Becker et al., 2009], sub-sampled at 4-arc-min. resolution. A 30-hr propagation forecast for the Pacific basin at 4-arc-min. basin can be completed in about 5 min., using a generic 12-CPU Linux server.

The model can take various forms of forcing input. The simplest forcing is a single rectangular fault with a uniform slip of any focal mechanism. The fault length and width are computed according to the empirical formulas of Wells and Coppersmith (1994). The seafloor deformation is computed according to Okada (1985). Following the common practice in tsunami modeling, we assume the ocean is initially at rest (zero velocity) and assume an instantaneous translation of the seafloor deformation to the sea surface. Namely, the initial sea surface deformation takes the same shape as the seafloor deformation. The model can also take finite fault solution as forcing with an arbitrary number of sub-faults. In this case, the Okada (1985) formula of seafloor deformation is computed for each sub-fault and the deformation is instantaneously added to the sea surface elevation at the end of rupture for each sub-fault (or at time = time of rupture + rise time).

The observed tsunami data at the DARTs are processed to remove the tides. This is done by subtracting low order tidal harmonic fit from the raw data that has a 1-min. sampling interval. This detiding method is not perfect and the detided trace can have a small non-zero offset (typically about 1 cm or so) well before the actual tsunami arrival. We subtracted the non-zero offset from the detided trace such that the detided trace is more or less at the zero value well before the tsunami arrival.

3.2 February 27, 2010 Chile tsunami

During the 2010 Chile tsunami, the RIFT model was run in real-time using the USGS W-phase centroid moment tensor solution (for the W-phase method, see Kanamori and Rivera, 2008; Hayes et al, 2009). The parameters used are: magnitude Mw=8.8 (Mo=2.0×10^{22}Nm), centroid 35.826 S. 72.668 W, Depth=35 km, strike=16, dip=14, rake=104. The length and width of the fault are 483.1 km and 99.5 km, respectively. With a shear modulus of 45 GPa, the uniform slip is 9.22 m. We were able to obtain real-time Pacific-wide propagation solution before the tsunami wave reached the nearest live DART 32412 (Foster et al. 2012). Unfortunately, the RIFT model was only integrated for 24 hours during the event, just before the tsunami peak arrival at the farthest DART (52405), so we reran the model for 30 hours for this study, using exactly the same parameters we used during the event. The results are the same except that we now have a longer time series. We label this run as "without depth-correction". To implement the dispersion relation (4), we ran RIFT with exactly the same forcing used during the event, but the ocean depth was replaced by the effective depth, defined by (5). We label this run as "with depth-correction".

Figure 4 compares the time series of model results without depth-correction (blue), with depth-correction (red), and the observed tsunami waveforms (black) at various DARTs across the Pacific. The DARTs are selected such that there is a good coverage of distance and azimuth (the locations and data of the DARTs can be found at NOAA's National Data Buoy Center: http://www.ndbc.noaa.gov/dart.shtml. The locations of DART used are also plotted in Figure 6.). The DARTs are listed in the order of observed tsunami arrival times. Without depth-correction, the difference between the modeled and observed tsunami arrival times at the DARTs got progressively worse as the distance (in terms of tsunami travel time) from the epicenter increased (compare blue with black lines, Figure 4). With depth-correction (red), the difference is substantially reduced, compared to the model run without depth-correction (blue). The modeled tsunami arrival times now more or less match those of the observed at most of the DARTs (compare red and black lines), judging by the initial tsunami arrival, time of peak, or overall fit for later arriving waves.

For DART 51407 (near Hawaii, Figure 4h), the observed and modeled tsunami arrivals with depth-correction (red) are about the same, in contrast to the 8-min. discrepancy without depth-correction (blue, also see Figure 1c). The most dramatic improvement is for DART 52405. With depth-correction, the modeled waveform is now in phase with that of the observed, rather than being out of phase (Figure 4l, also see Figure 1e).

Despite the overall improvement of tsunami arrival time with depth-correction, there are significant differences between the modeled and observed tsunami waveforms at some DARTs. It is worth noting that the wave period of the modeled tsunami at DART 51406 is somewhat larger than that of the observed, such that the second peak does not line up with that of the observations (Figure 4b).

We note that the modeled waveform for DART 54401 differs significantly from that of the observed and the waveform without depth-correction seems match better overall to the observed,

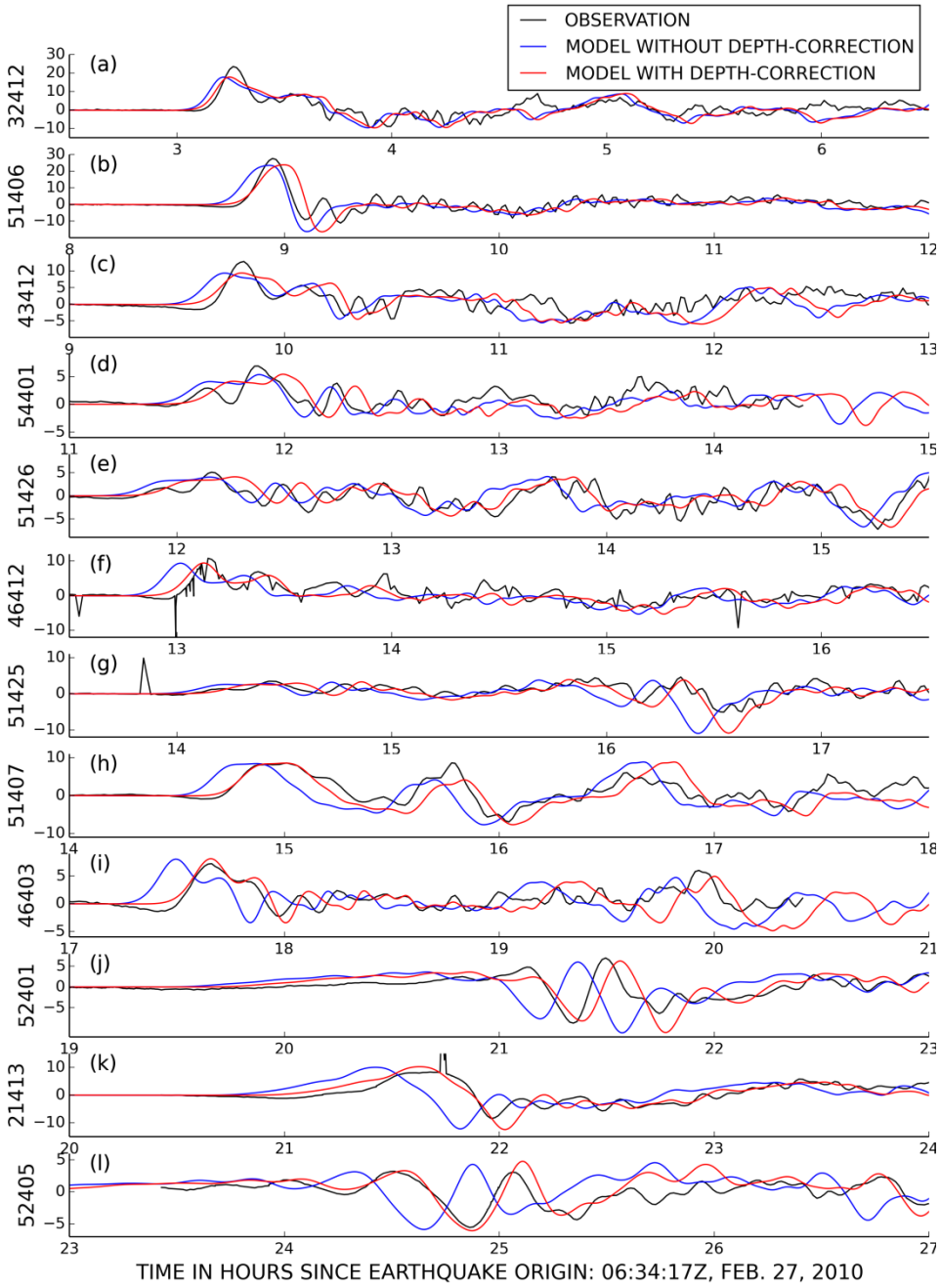

Figure 4. Comparison of model runs with (red) and without (blue) depth-correction with observations (black) at DARTs for the 2010 Chile tsunami. See Section 3.2 for details of forcing parameters used.

although with depth-correction, the initial arrival time seems to match the observation better (Figure 4d). The same can be said of DART 51246 (Figure 4e). The mismatch of the waves might be

attributable to the source model error. Even using a finite fault solution with DART inversion, Watada et al. (2014) was unable to reproduce the observed waveform at DART 51426.

It is worth noting that the first arriving waves are much smaller than later arriving waves at some DARTs. For example, maximum wave amplitudes occurred about two hours after the initial arriving waves at 51425 and 52401 (Figure 4g and Figure 4j). For these locations, it is more important that the modeled waveforms match the observed ones at the times of maximum wave amplitude. With depth-correction, the times of the maximum wave amplitudes do match better with the observed (near hour 16.3 for DART 51425 and near hour 21.5 for DART 52401. Figure 4g, j).

With depth-correction, it appears that only the phase of the tsunami wave is altered but the amplitude and shape of the tsunami remain unchanged. To take a closer look, we compare the model time series of sea level with and without depth-correction at the DARTs, shown in Figure 5. The time axis for the run without depth-correction is shifted from about 1 minute for the nearest DART (32412) to the epicenter to about 14 minutes for the farthest DART (52405). The time shifts needed to line up the model runs with and without depth-correction are also indicated in Figure 5. For the first few hours after the tsunami arrival, there is almost no difference between the time series with and without depth-correction, after adjusting for the tsunami arrival time. As time goes on, small differences begin to emerge. This is understandable because the difference in tsunami travel time will eventually have some effects on the wave fields, even in the open ocean, because travel time changes will lead to differential changes in wave reflection, scattering, and refraction, because of the complexities of the ocean bathymetry.

So far we only compared model results with and without depth-correction for a dozen DARTs. To get a sense of how depth-correction alters the tsunami wave basin wide, we show in Figure 6a,b the absolute difference and relative difference (percent) between the maximum wave amplitudes with and without depth-correction. The locations of the DARTs used for the comparison discussed above are also indicated (black triangles). The black square indicates the epicenter of the earthquake. For the vast areas of the deep open ocean, the absolute difference is less than 0.5 cm or relative difference is less than 10% (blue or cold color). Larger differences occur near the coastline and in areas where the depth is relatively shallow or in areas with complex topographic features, such as the low-latitude region of the western Pacific, the east of New Zealand, and the southwest Pacific. Differences as large as 100% are seen in the East China Sea. Large differences are also seen in the Arafura Sea (north of Australia). We need to point out that 30 hours of integration might not be long enough for waves to fully propagate into these regions. We should also note that tsunami waves in regions with water depth less than 500 m cannot be well resolved by the numerical model at 4-arc-min. resolution. For example, the wavelength for a 10-min. period wave for an ocean depth of 500 m is 42 km, covering only 5 to 6 model grid points. Thus, the numerical solution itself is questionable for these regions, where the water depth is only a few tens of meters. Interestingly, all the DARTs happened to be located in regions with small differences in percentage terms (Figure 6b).

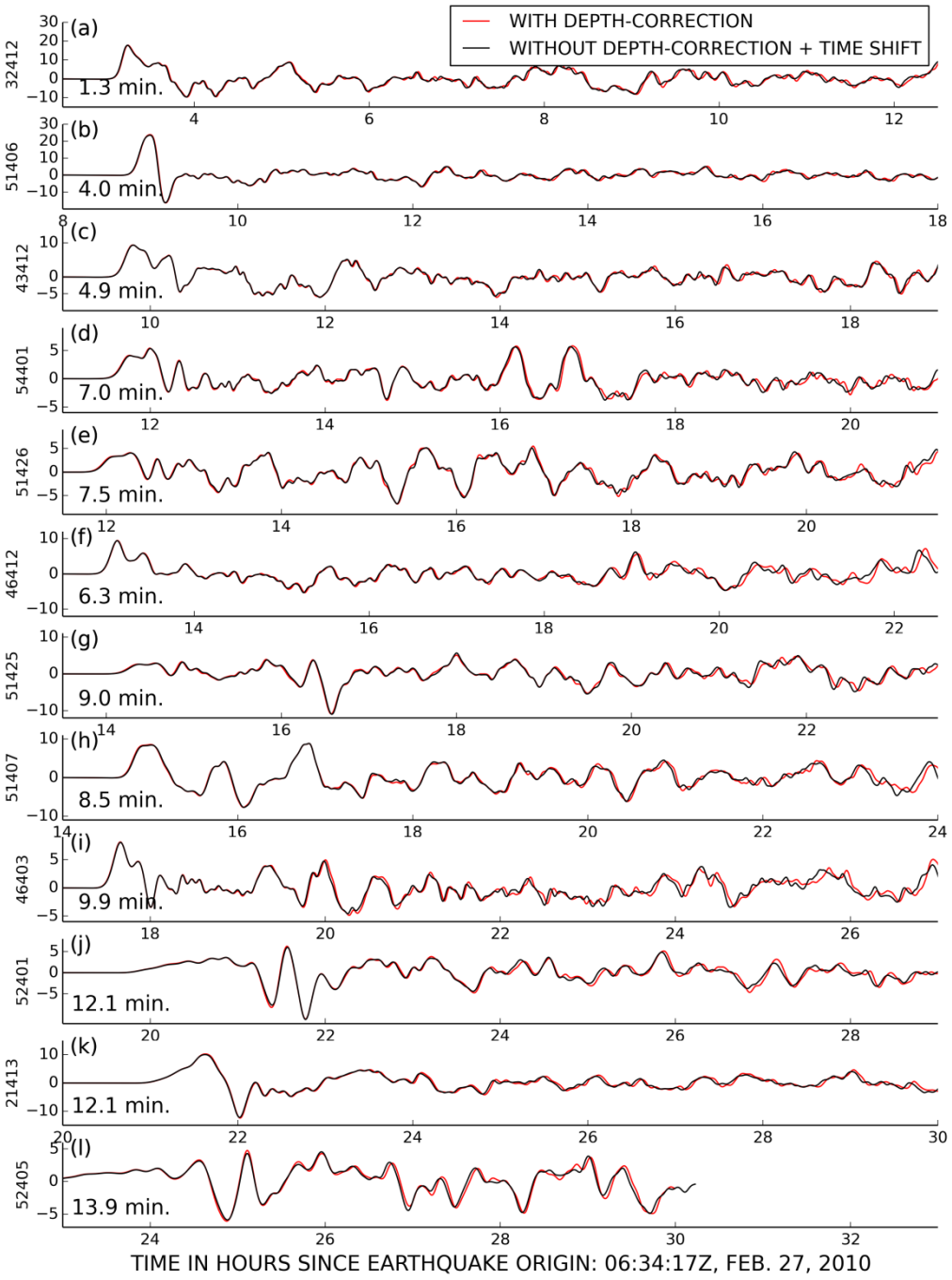

Figure 5 Comparison of model runs with (red) and without (black) depth-correction for the 2010 Chile Tsunami. The time axis for model run without depth-correction for each DART is shifted to line up the initial tsunami arrival with model run with depth-correction. The time shift varies from 1.3 min. for DART 32412 to 13.9 min. for DART 52405.

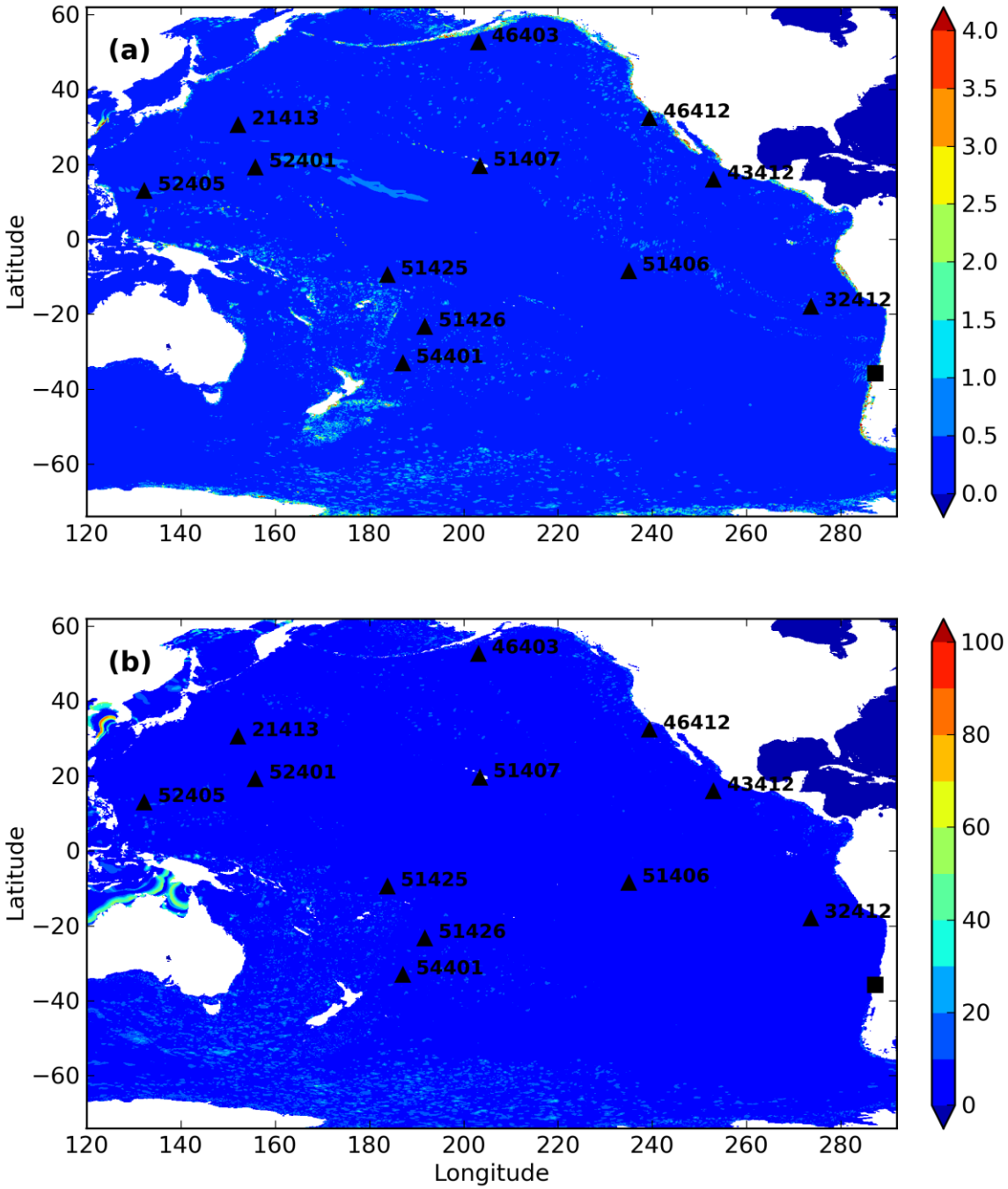

Figure 6 (a) Absolute difference (in cm) and relative difference (in percent) of maximum wave amplitude between model runs with and without depth-correction for the 2010 Chile tsunami. The locations of DARTs used in the model-observation comparison are also shown (black triangles). The Epicenter is indicated by the black square.

3.3 March 11, 2011 Tohoku tsunami

During the 2011 Tohoku tsunami, the RIFT model was run in real-time using a centroid moment tensor solution from the Global CMT Project (Dziewonski et al. 1981; Ekström et al. 2012, https://www.ldeo.columbia.edu/research/seismology-geology-tectonophysics/global-cmt), with a rectangular fault and uniform slip. The result was helpful during the event for PTWC's operations. Unfortunately, the result is not suitable for this travel time study, because even the tsunami arrival time at the nearest DART (21418) was several minutes earlier than that of the observed. This difference cannot be corrected by the depth-correction method. This suggests that a uniform slip of a rectangular fault is too crude to represent the sources of the Tohoku tsunami. We therefore forced the RIFT model with the USGS finite fault solution for this study. The USGS finite fault solution consists of 325 25-km by 20-km sub-faults, with a total fault area of 625 km by 260 km. (http://earthquake.usgs.gov/earthquakes/eqinthenews/2011/usc0001xgp/finite_fault.php).
The rupture time of the sub-faults varies from 14 to 230 seconds and the rise-time varies from 9 to 26 seconds. This sub-fault solution amounts to a moment magnitude of 9.0.

Figure 7 compares model results without depth-correction (blue), with depth-correction (red), and observation (black) at DARTs. Again, the DARTs are selected to have a good coverage of distance and azimuth. Without depth-correction, the difference between the modeled and observed tsunami arrival times at the DARTs got progressively worse as the distance from the epicenter increased (compare blue and black curves). With depth-correction (red), the difference is substantially reduced, compared to the model run without depth-correction. For DART 21418, the tsunami waveforms with and without depth-correction showed little difference (Fig. 7a). This is because the DART is only a few hundred km from the source region. The tsunami arrived at DART 52405 after about 3.5 hours (Fig. 7c). At first glance, the model results with and without depth-correction do not seem to show much difference. A closer look however, reveals the arrival times differ by about 3 min, judging by the times of the peak tsunami amplitude.

The modeled tsunami still arrives 2-4 min. too soon compared to the observed for the furthest DARTs (43412, 32412, 32401, see Figure 7j, k, l), although the discrepancies are reduced substantially compared to the case without depth-correction. For example, without depth-correction, the second peak of the modeled tsunami at DART 32401 almost lines up with the first peak of the observed (compare blue and black in Figure 7l), whereas with depth-correction, the first peak from the model lines up with the observed first peak much better (compare red and black in Figure 7l).

For the 2011 Tohoku tsunami, the depth-correction approach cannot fully explain the discrepancies between the modeled and observed tsunami arrival times. We note some important differences between the two tsunamis. Although the Tohoku tsunami was generated by a larger earthquake, magnitude 9.0 vs. magnitude 8.8, the wave periods are somewhat shorter, as revealed in the spectral analysis of Yamazaki et al. (2011; 2012). Physical dispersion, which is lacking in our model, might have some effects on the modeled tsunami arrival times and might explain part of the remaining discrepancies. We also note we assumed the seafloor deformation is instantly translated to the sea surface deformation. In reality, there might be a finite time of adjustment. So the true discrepancies between the observed and modeled tsunami arrival times might be smaller than shown.

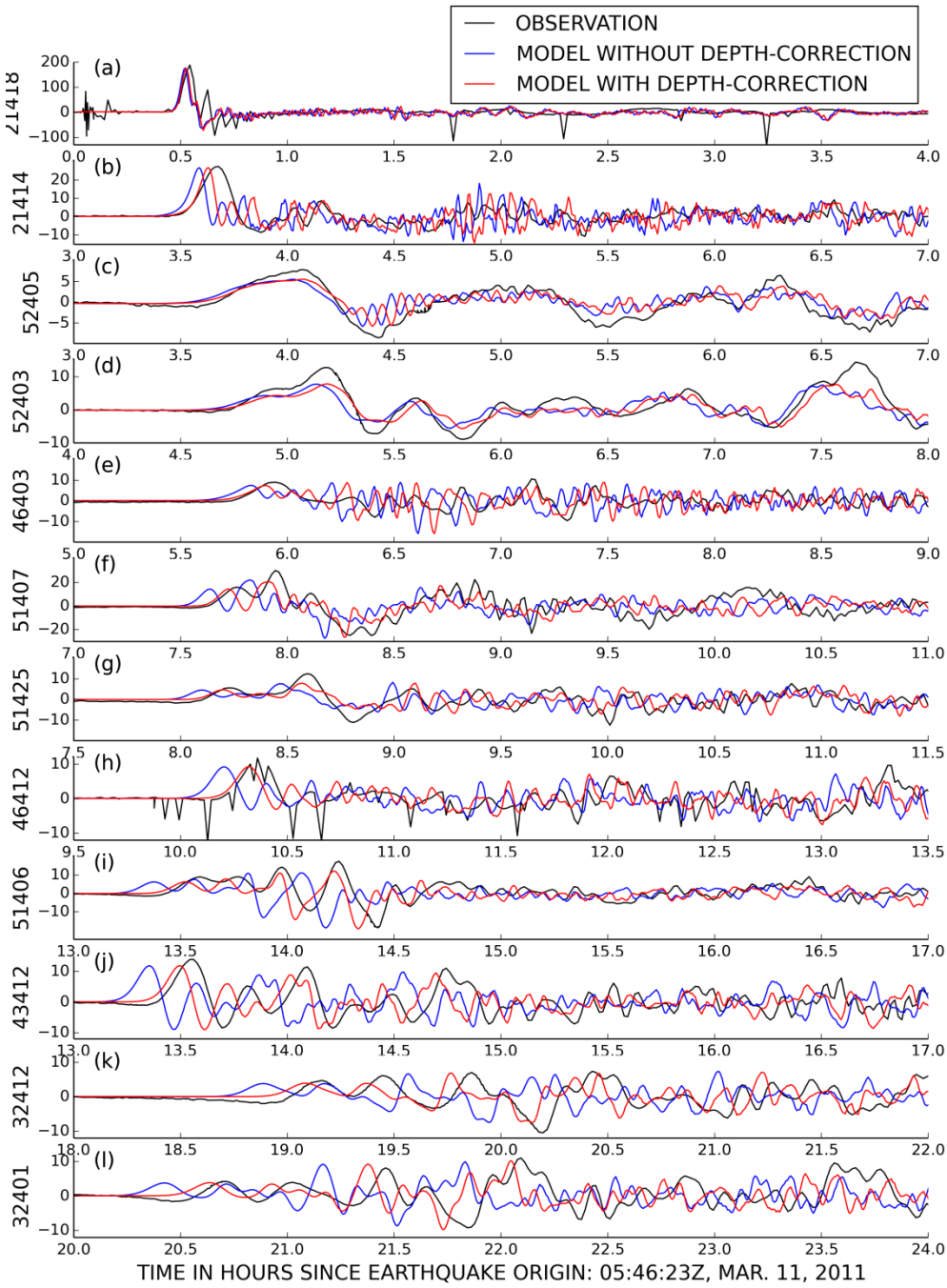

Figure 7. Comparison of model runs with and without depth-correction with observations at DARTs for the 2011 Tohoku tsunami. See Section 3.2 for details of forcing parameters used.

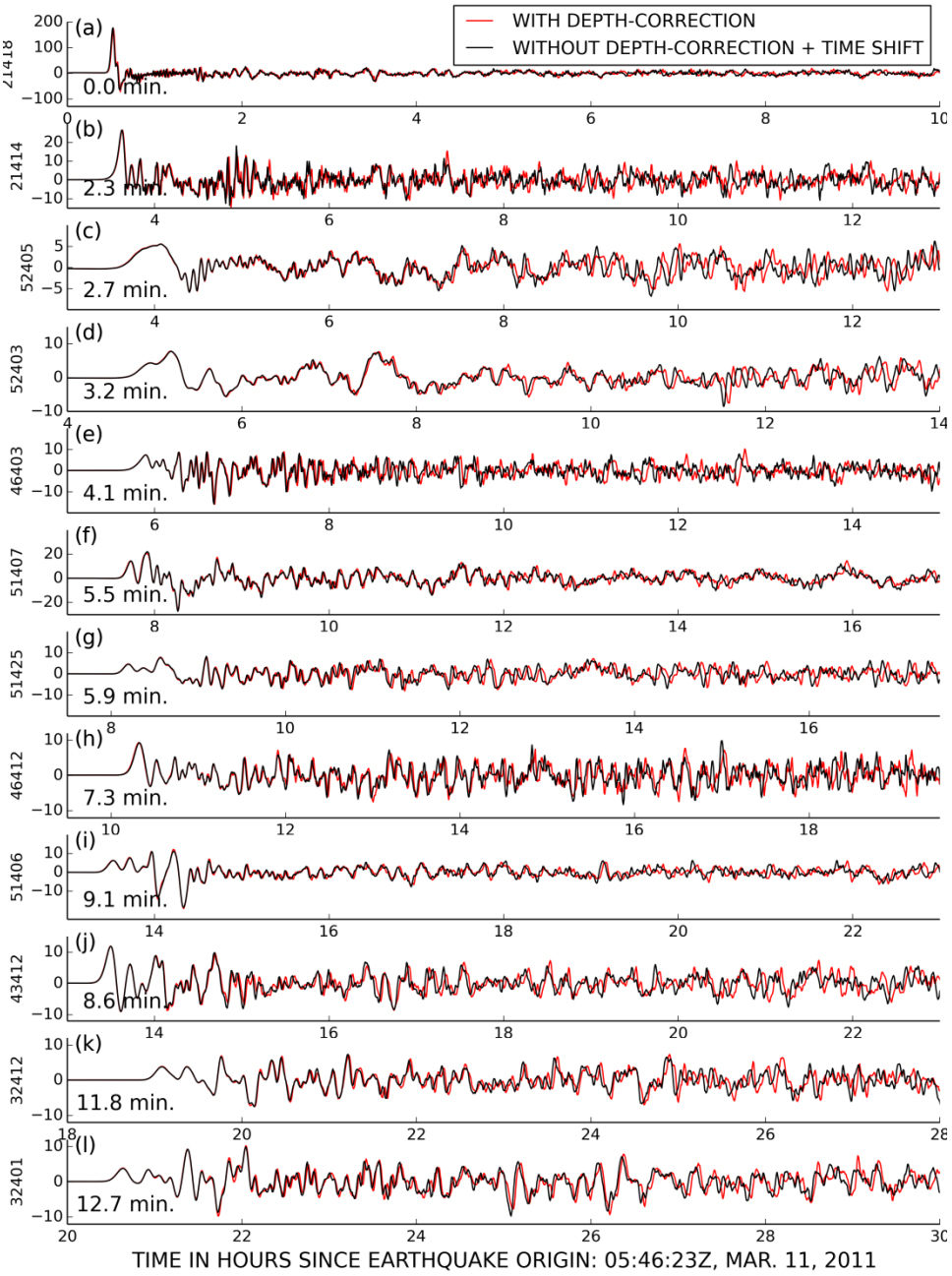

Figure 8. Comparison of model runs with (red) and without (black) depth-correction, for the Tohoku 2011 tsunami. The time axis for model run without depth-correction is shifted to line up the initial tsunami arrival with the model run with depth-correction. The time shifts (in minutes) needed to line up the two runs are indicated in the plots.

As for the case of 2010 Chile tsunami, we want to know whether or not depth-correction alters the tsunami wave forms, other than shifting the tsunami arrival times. Figure 8 compares the time series of model results at the DARTs with and without depth-correction. The time axis of the model run without depth-correction is shifted between 0 and 13 min. to line up with the tsunami arrival times of the model run with depth-correction (the time shifts are listed in Figure 8).

For the first two hours, there is almost no difference between the two model runs, after adjusting the time axis. Once again, depth-correction does little to the early direct arriving tsunami waves in the deep ocean other than shifting the tsunami arrival times. But as time goes on, the differences begin to appear. At DART 46403, for example, the waveforms with and without depth-correction have substantial differences (Figure 8e, near hour 13). Similar patterns can be seen at other DARTs.

Figure 9a, b show the absolute and relative difference of the maximum wave amplitude between the two model runs with and without depth-correction. The locations of the DARTs used for the comparison are also indicated (black triangles). The black square indicates the epicenter of the earthquake. For most areas of the open deep ocean, the difference is less than 1 cm (blue or cold color) or less than 10% in percentage terms. Again, larger differences occur near the coastline and in areas where the depth is shallow or in areas with complex topographic features, such as the low-latitude region of the western Pacific and east of New Zealand. Relatively large differences can also be seen in some areas of the deep ocean. For example, the differences are about a 3-4 centimeters near the Kuril Trench and off the east coast of Japan (Figure 9a, upper-left corner). Overall, the absolute difference is larger than that of the 2010 Chile tsunami (compare Figure 6a and Figure 9a). The relative difference (percentage-wise) however, is rather similar. Note the elevated absolute difference shown near Kuril Trench and along the great circle from Japan to South America do not show up in relative difference (compare Figure 9a with Figure 9b). For the southern ocean, the 2011 Tohoku tsunami does show somewhat larger relative difference, up to 30-40% (south of Australia). The regions of large differences are fragmented and mixed with regions of small differences (e.g., south of Australia). Again, at 4-arc-min. resolution, our model cannot resolve tsunami waves in shallow waters. The difference between model runs with and without depth-correction in areas with an ocean depth less than 500 m will not be very meaningful. Much higher resolution or nested-grid approach is needed to further study the true effects of depth-correction in shallow waters.

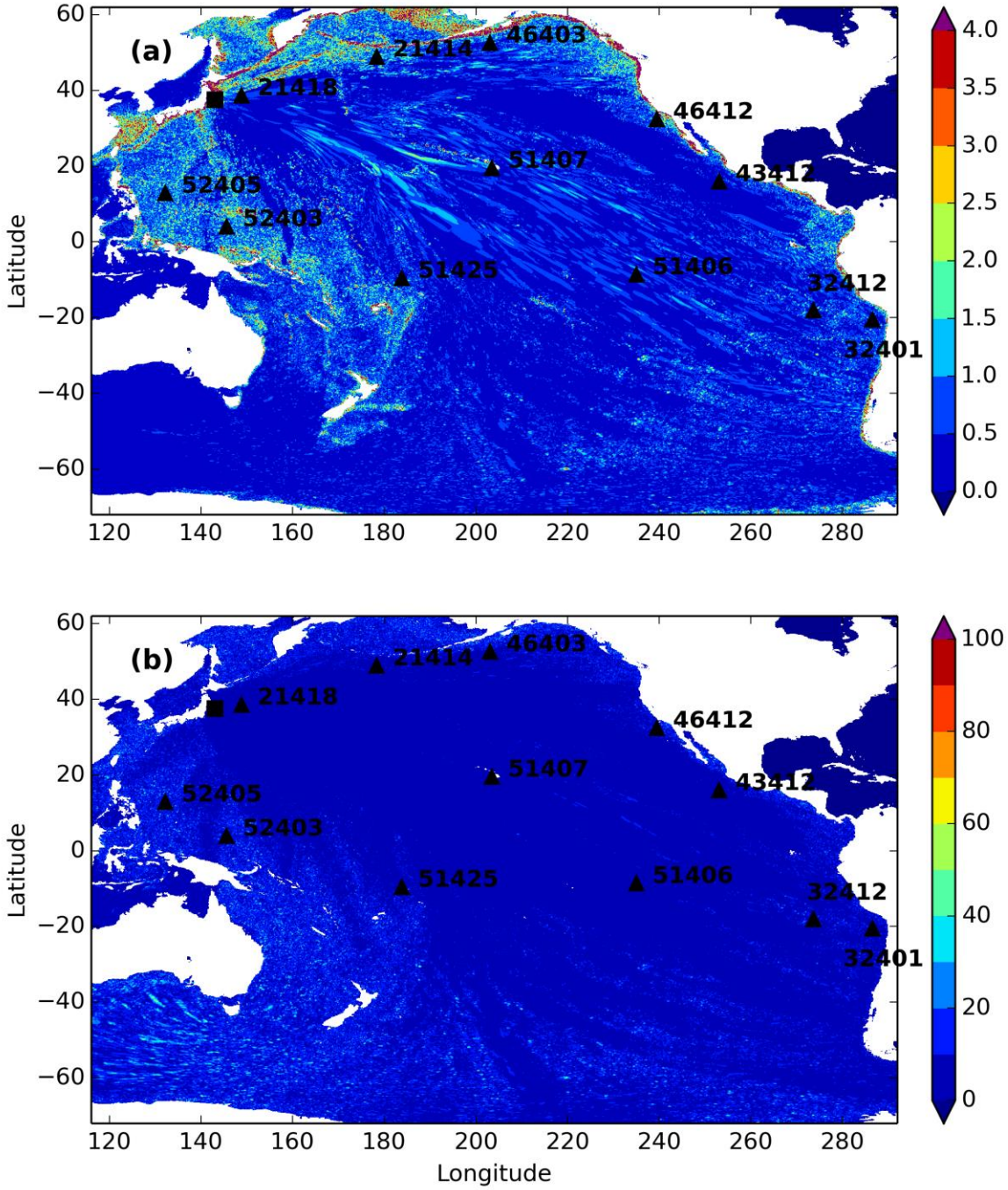

Figure 9. (a) Absolute difference (in cm) and (b) relative differences (in percent) of maximum wave amplitude between model runs with and without depth-correction for the 2011 Tohoku tsunami (unit: cm). The locations of DARTs used in the model-observation comparison are also shown (black triangles). The Epicenter is indicated by the black square.

4. **Conclusions**

We proposed a simple ocean depth-correction method to reduce the discrepancies of the modeled and observed tsunami arrival times. The method is based on the dispersion relation of shallow water surface gravity waves in a compressible homogenous fluid. The phase speed of surface gravity waves is reduced in such a system. Implementation of this method is straightforward by replacing the ocean bathymetry used in numerical models by the effective bathymetry, according to formula (5). There is no need to modify the numerical codes of the existing tsunami models (i.e., there is no extra computational cost). Although our method does not take into account the full physics of the interaction of the ocean and the elastic earth, it can be interpreted as a bulk-parameterization of these effects. We applied this approach to the 2010 Chile and 2011 Tohoku tsunamis with forcing purely derived from seismic data and found that the depth-correction can account for most of the discrepancies between the modeled and observed tsunami arrival times. Discrepancies of 3-4 min. still remain for the 2011 Tohoku tsunami.

The depth-correction approach did not seem to alter the behavior of the direct arriving tsunami waves (waveforms and amplitudes) at DARTs within a couple hours of tsunami arrival, other than shifting the tsunami arrival times to match better with observations. However, substantial differences still occur in regions of shallow water and regions of complex bathymetry. This depth-correction method can potentially be used to improve the accuracy of tsunami source inversion by improving tsunami arrival times at far field DARTs. Basin wide, the differences between runs with and without depth-correction are less than 10% over most part of the deep ocean. To accurately assess the effects of depth-correction on coastal run-ups however, resolution capable of resolving inundation is needed.

Errors in model tsunami arrival times can arise from the inaccuracies of the source models. For example, Allgeyer and Cummins (2014) showed that source models derived from fitting model to observed tsunamis result in smaller tsunami travel time errors. Errors in model numerics can also contribute to the tsunami arrival time error. Shallow water equations might not be suitable for events with short tsunami wave periods or wavelengths. Most if not all tsunami forecast models (for warning purposes, at least) in use today are based on shallow water equations, without resolving the physical dispersion of tsunami waves. Different numerical codes can also have different characteristics of numerical errors (numerical dispersion and dissipation, etc.). Even if the same travel time correction method is used, the numerical results from different models might be different.

As a final remark, we note that although the depth-correction method proposed in this study is simple and easy to implement, it has its limitations because it does not account for the full physics that affect tsunami travel time. We were not able to reproduce the small initial depression observed (although the small initial depression is of no consequence as far as tsunami warning is concerned). However, taking into account fully the physics influencing tsunami travel time might require integrating a coupled ocean and elastic earth system. The ocean component of the coupled system might have to be a non-hydrostatic, compressible, and baroclinic ocean model or a model capable of representing these effects. Such a coupled model will be unfeasible for the foreseeable future, at least for tsunami warning purposes.

Acknowledgements

We thank Dr. Stuart Weinstein and Dr. Gerard Fryer of PTWC for helpful discussions and comments. We thank the National Data Buoy Center (NDBC) for maintaining the DART network and for providing the DART data. We also thank Gavin Hayes of US Geological Survey for providing the W-phase CMT solution for the 2010 Chile earthquake and the finite fault solution of the 2011 Tohoku earthquake. Editorial assistance from Juleen Wong is greatly appreciated.

References

Allgeyer, S. and P. Cummins (2014), Numerical tsunami simulation including elastic loading and seawater density stratification, Geophys. Res. Lett., 41, doi:10.1002/2014GL059348.

Arakawa, A. and V. Lamb (1977): Computational design of the basic dynamical processes of the UCLA general circulation model, Methods in Computational Physics, Vol. 17, 174-267.

Becker, J. J., D. T. Sandwell, W. H. F. Smith, J. Braud, B. Binder, J. Depner, D. Fabre, J. Factor, S. Ingalls, S-H. Kim, R. Ladner, K. Marks, S. Nelson, A. Pharaoh, R. Trimmer, J. Von Rosenberg, G. Wallace and P. Weatherall (2009): Global Bathymetry and Elevation Data at 30 Arc Seconds Resolution: SRTM30_PLUS, Marine Geodesy, 32:4, 355-371, DOI: 10.1080/01490410903297766

Dziewonski, A. M., T.-A. Chou and J. H. Woodhouse, Determination of earthquake source parameters from waveform data for studies of global and regional seismicity, J. Geophys. Res., 86, 2825-2852, 1981. doi:10.1029/JB086iB04p02825

Ekström, G., M. Nettles, and A. M. Dziewonski (2012): The global CMT project 2004-2010: Centroid-moment tensors for 13,017 earthquakes, Phys. Earth Planet. Inter., 200-201, 1-9. doi:10.1016/j.pepi.2012.04.002

Foster, J. H., B. A. Brooks, D. Wang, G. S. Carter and M. A. Merrifield (2012): Improving Tsunami Warning Using Commercial Ships. Geophys. Res. Lett, doi:10.1029/2012GL051367

Grilli, S. T., J.C. Harris, T. S. T. Bakhsh, T. L. Masterlark, C. Kyriakopoulos, J.T. Kirby, and F. Shi (2012): Numerical simulation of the 2011 Tohoku tsunami based on a new transient FEM co-seismic source: Comparison to far- and near-field observations, Pure Appl. Geophys, doi:10.1007/s00024-012-0548-y.

Hayes, G. P., L. Rivera, and H. Kanamori (2009): Source inversion of W phase: Real time implementation and extension to low magnitudes, Seismol. Res. Lett., 80(5), 817–822, doi:10.1785/gssrl.80.5.817.

Inazu, D. and T. Saito (2013): Simulation of distant tsunami propagation with a radial loading deformation effect, Earth Planets Space, Vol. 65, 835-842.

Kanamori, H. and L. Rivera (2008): Source inversion of W phase: Speeding up seismic tsunami warning, Geophys. J. Int., 175, 222–238, doi:10.1111/j.1365-246X.2008.03887.x.

Kato, T., Y. Terada, H. Nishimura, T. Nagai and S. Koshimura (2011): Tsunami records due to the 2010 Chile Earthquake observed by GPS buoys established along the Pacific coast of Japan. Earth, Planets, and Space, 63, e5–e8.

Kono, Y., S. Takata, F. Imamura, K. Minoura (2002): Numerical Analysis on Johgan Tsunami by Using Fault Model in Consideration of the Origin of Miyagi-Ken-Oki Earthquake. The 5th International Conference on Hydro-Science and Engineering, Warsaw, Poland, September 2002.

Okada, Y. (1985): Surface deformation due to shear and tensile faults in a half space, Bull. Seismol. Soc. Am., Vol. 75, 1135-1154.

Okal, E. A. (1982): Mode-wave equivalence and other asymptotic problems in tsunami theory. Phys. Earth Planet. Inter., Vol. 30, 1-11.

Ray, R.D. (1998): Ocean self-attraction and loading in numerical tidal models, Marine Geodesy, Vol. 21, No. 3, 181-192, DOI: 10.1080/01490419809388134

Saito, T., Y. Ito, D. Inazu and R. Hino (2011): Tsunami source of the 2011 Tohoku - Oki earthquake, Japan: Inversion analysis based on dispersive tsunami simulations, Geophys. Res. Lett., 38, L00G19, doi:10.1029/2011GL049089.

Shchepetkin, A. F. and J. C. McWilliams (2011): Accurate Boussinesq oceanic modelling with a practical, "stiffened" equation of state. Ocean Modelling, Vol. 38, pp. 41-70.

Tsai V.C., J.P. Ampuero J.P., Kanamori H., and D.J. Stevenson D.J., (2013): Estimating the effect of Earth elasticity and variable water density on tsunami speeds. Geophy. Res. Lett, Vol. 40, 492-496, doi:10.1002/grl.50147.

Wang, D., D. Walsh, N. Becker, and G. Fryer (2009): A methodology for tsunami wave propagation forecast in real time, EOS Trans AGU, 90(52), Fall Meet. Suppl., Abstract OS43A-1367.

Wang, D., et al. (2012), Real-time forecasting of the April 11, 2012 Sumatra tsunami, Geophys. Res.

Lett., 39, L19601, doi:10.1029/2012GL053081.

Ward, S. N. (1980): Relationships of tsunami generation and an earthquake source. J. Phys. Earth, vol. 28, 441-474.

Watada, S., K. Satake, Y. Fujii (2011): Origin of traveltime anomalies of distant tsunami, in Abstract NH11A-1363 presented at 2011 Fall Meeting, AGU, San Francisco, Calif., 5-9 Dec

Watada, S. (2013), Tsunami speed variations in density-stratified compressible global oceans, Geophys. Res. Let., 40, 4001-4006, doi:10.1002/grl.50785.

Watada, S., S. Kusumoto, and K. Satake, (2014): Traveltime delay and initial phase reversal of distant tsunamis coupled with the self-gravitating elastic earth. J. Geophys. Res., Solid Earth, Vol. 119, No. 5, pp. 4287–4310, DOI: 10.1002/2013JB010841.

Wells, D. L. and K. J. Coppersmith (1994), New empirical relationships among magnitude, rupture length, rupture width, rupture area, and surface displacement, Bull. Seismol. Soc. Am., Vol 84, 974-1002.

Yamamoto, T. (1982), Gravity waves and acoustic waves generated by submarine earthquakes, Intl. J. Soil Dyn. Earthq. Eng., 1, 75-82.

Yamazaki, Y., K. F. Cheung (2011): Shelf resonance and impact of near-field tsunami generated by the 2010 Chile earthquake. Geophys. Res. Lett., Vol. 38, L12605, doi:10.1029/2011GL047508.

Yamazaki, Y., K. F. Cheung, G. Pawlak and T. Lay (2012): Surges along the Honolulu coast from the 2011 Tohoku tsunami, Geophys. Res. Lett., 39, L09604, doi:10.1029/2012GL051624.

Yasuda, T. and H. Mase (2013): Real-time tsunami prediction by inversion method using offshore observed GPS buoy data: Nankaido. J. Waterways, Port, Coastal, and Ocean Engineering, Vol. 139, No. 3, pp. 221-231.

ISSN 8755-6839

SCIENCE OF **TSUNAMI HAZARDS**

Journal of Tsunami Society International

Volume 34 **Number 1** **2015**

THE SPATIAL-TEMPORAL DISTRIBUTIONS OF THE TSUNAMIGENIC EARTHQUAKE SOURCES

Boris Levin[1], Elena Sasorova[2]

[1]Institute of Marine Geology and Geophysics of RAS, Yuzhno-Sakhalinsk-693022, Russia
[2]Shirshov Institute of Oceanology of RAS, Moscow- 117991, Russia

ABSTRACT

The spatial-temporal periodicity and occurrence of tsunamigenic earthquakes continue to be one of the still unsolved fundamental problems that also may have great practical operational importance. Thus, for the present investigation, we used data of tsunamigenic earthquakes (TEQ) of the last 120 years. All of the TEQ events with tectonic origin and magnitude M≥7.5, intensity of tsunami I>=1, and validity of event V=4, were selected in a working catalog which was prepared on the basis of the *Expert Tsunami Data Base for the Pacific*, and the *Tsunami Event and Runup Database* of NOAA. The total number of chosen events for the study, was 99. For these events, we analyzed the spatial and spatial-temporal distributions of the TEQ density and of released energy separately for the entire Earth, the Northern and Southern hemispheres, and for several regions of the Pacific Basin (Aleutian Islands, Kuril Islands, the equatorial belt and Central America and South America). The analysis of distribution of the TEQ in time, reveals a sharp increase in activity (density of events and of released energy) in the early 20th and 21st centuries. However, the most complete benefit of the study was the determination of the two-dimensional distribution of events (in latitudes and in time). The analysis revealed periodic changes of TEQ activity in different time intervals. The intensification of tsunami activity appears to have different periodicity at various latitudinal belts. We determined that tsunami sources are located basically in three latitudinal intervals: 40°N – 60°N, 15°N – 10°S and 25°S-35°S. The periodicity of tsunami activity varied from 10 to 50 years.

Keywords: *tsunamigenic earthquake, spatial-temporal periodicity, two-dimensional distribution of events.*

Vol. 34, No. 1, page 23 (2015)

1. INTRODUCTION

The spatial-temporal periodicity of the occurrence of tsunamigenic earthquakes continues to be one of the unsolved fundamental problems that may have great practical importance. It is known that the Earth's seismic activity demonstrates a distinct unevenness (irregularity) in both space and time. The periods of the seismic activity (SA) increases are followed by periods of decreases. These periods manifest themselves differently at different regions of the Earth. An increase of seismic activity in one region may correspond to a decrease in another region.

The objective of the present study was to examine the spatial-temporal distributions of tsunamigenic earthquakes sources. Specifically, we considered only tectonic tsunamis (caused by strong earthquakes). Such tsunamigenic earthquakes tend to have a magnitude (M) which is greater than or equal to 7.5. Therefore to analyze the spatial and temporal distributions of tsunamigenic earthquakes (TEQ) we had to use sufficiently long series of reliable observational data. For that reason we chose to study the TEQ over the last 118 years (from 1895 to 1913). Furthermore considered were only tectonic tsunamis in which the intensity (I) of tsunami waves was greater or equal than one. We chose the value I> = 1, since until 1950 there was not enough reliable observations of weaker events for the Pacific. We analyzed the spatial and spatial-temporal distributions of the TEQ density and released energy separately for the entire Earth, for the Northern and Southern hemispheres, and for several regions of the Pacific Basin (Aleutian Islands, Kuril Islands, the equatorial belt, Central America, and South America).

2. SELECTION OF OBSERVATIONAL DATA, AND PREPROCESSING

The working catalog of tsunamigenic earthquakes was prepared on the basis of the Expert Tsunami Data Base for the Pacific (HTDB/WLD 2010), and the Tsunami Event and Runup Database at NOAA (NGDC/NOAA 2010). To analyze the spatial and temporal distributions of tsunamigenic earthquakes (TEQ) we had to use sufficiently long series of reliable observational data. Therefore we studied TEQs of the last 118 years (from 1895 to 1913).

We took into account that from 1900 to 1963 the errors in the determination of earthquake magnitude was ± 1, the error in determining the intensity of tsunami waves (I) for HTDB / WLD was equal to ± 0.2, and for weak tsunamis with -4 <= I <= 0 error was ± 1. (Gusiakov 2011). This was the reason why we chose to study all TEQ of tectonic origin, with magnitude M≥7.5, intensity of tsunami I>=1, and event validity V=4.

Then, after removing duplicates, cross-checking and verifying the data from both databases, we selected events for the working catalog of tectonic tsunamis for which we carried out pre-processing procedures and recalculation to a single scale of magnitude values in the working directory (by conversion to Ms magnitude). This processing left 99 seismic events which were identified as sources of tectonically-generated tsunamis with intensities equal to or greater than 1.0. These events formed the basis of the working catalog for future research as well (hereafter called simply as a catalog or CTEQ).

In order to compare the spatial and spatial-temporal distributions of the TEQ and earthquakes (EQ) with M>= 7.5 were used from the working catalog of strong earthquakes for the period 1900 to 2013 (CSEQ) and used the following two versions of the catalog of NEIC (USGS/NEIC):

1. NEIC from 1973 to 2013,

2. Catalog of the Significant Worldwide Earthquakes (2150 B.C. - 1994 A.D.), compiled by USGS/NEIC on the basis of the NOAA agency's database.

The preliminary standardization of magnitudes and removal of aftershocks (more exactly the creation of a version of the working catalog without aftershocks) was carried out for the mentioned above subsets of events. The current version of the EQ catalog includes data on 620 strong global earthquakes over the past 113 years, i.e. almost since the beginning of instrumental seismic observations.

Subsequently, the temporal EQ distributions were calculated separately for eighteen latitudinal intervals (belts): 90°-80°N, 80°-70°N, 70°-60°N, 60°-50°N and so on (the size of each belt being equal to 10°). In both cases (for TEQ and for strong EQ) the entire range of observations was subdivided into several 5-year intervals. The total number of events and the total energy released by EQ were determined in each five-year interval.

Given the fact that earthquakes occur primarily along tectonic plate boundaries, the earthquake number and the released energy values were normalized by the length of the lithospheric plate boundaries in each chosen interval of latitude. Thus we obtained the density of seismic events and the density of released energy. These values gave us the average number of earthquakes generated for every 100 kilometers of the plate boundaries and the average value of the released energy by earthquakes (i.e. capability of this section of the tectonic boundary). These characteristics have a clear physical meaning, because they allowed us to compare the seismic activity of various parts of the globe.

Thus, we analyzed the spatial and spatial-temporal distributions of the TEQ density and released energy separately for the entire Earth, for the Northern hemisphere, for the Southern hemisphere and for several regions of the Pacific Basin (Aleutian Islands, Kuril Islands, the equatorial belt, Central America, and South America).

3. THE SPATIAL DISTRIBUTIONS OF THE EPICENTERS OF THE TSUNAMI EARTHQUAKES AND EPICENTERS OF THE EARTHQUAKES WITH M>=7.5

Figure 1 shows the distribution of epicenters for TEQs, which are listed in the catalog (CTEQ) on the map of the World Ocean, while Fig. 2 presents the location of the epicenters of strong EQs with M≥ 7.5, which are included in the other catalog (CSEQ). The total number of events located outside the Pacific amounts to 8 (i.e. 8% of the total number of events).

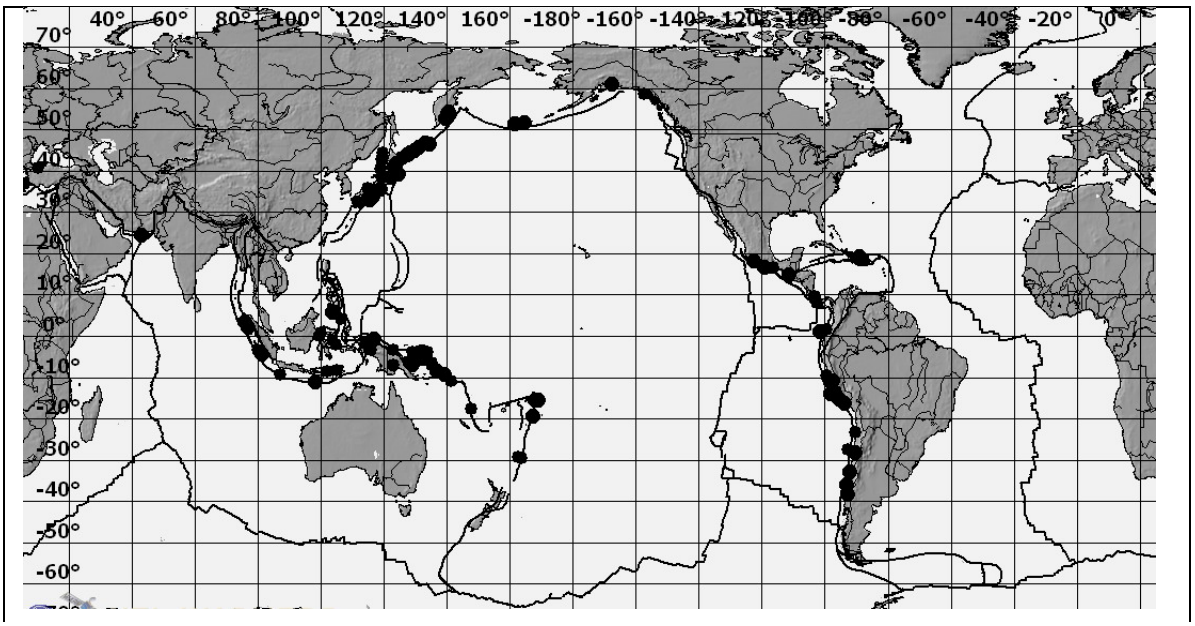

Figure 1. The distribution of the TEQ epicenters since 1895 on the world map. The epicenters are marked by black circles.

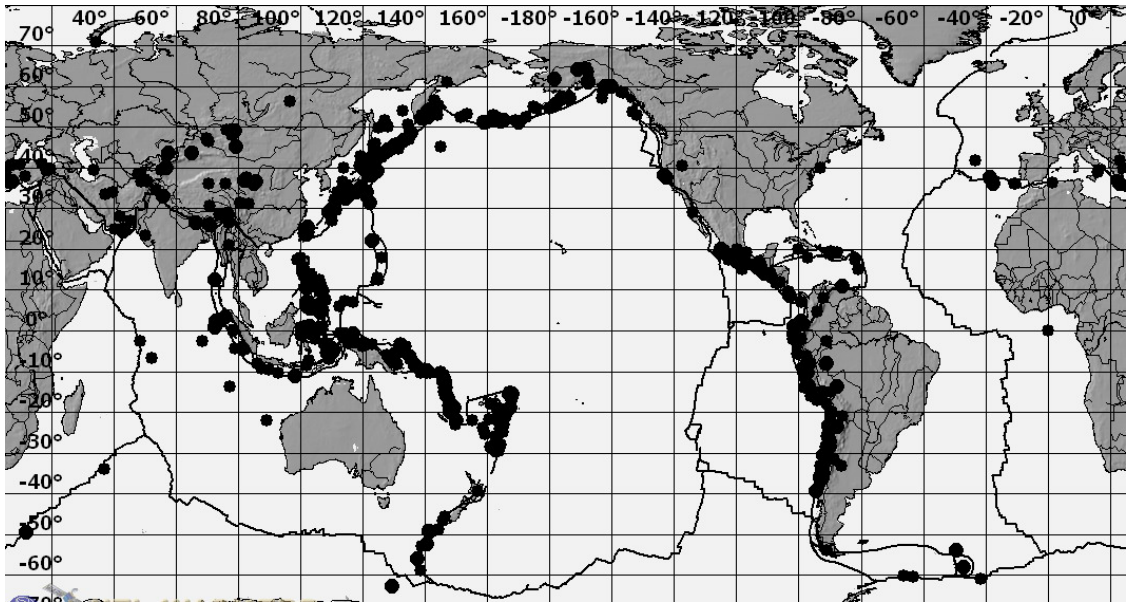

Figure 2. The distribution of the EQ with M ≥ 7.5 since 1895 on the world map. The epicenters are marked by black circles. The total number of the EQ amounts to 621

Analysis of the spatial distributions of the TEQ, as noted above, was based on the separation of the Earth's surface by 18 latitudinal belts (the size of latitudinal belt being equal to 10º). Fig. 3a shows the distribution of the TEQ number by latitude. On this distribution, clearly distinguished are two maxima at latitudes 40° - 50°N and 0° - 10°S, a local minimum in the vicinity of 20° - 30°N and practically zero values on the polar caps and in the high latitudes.

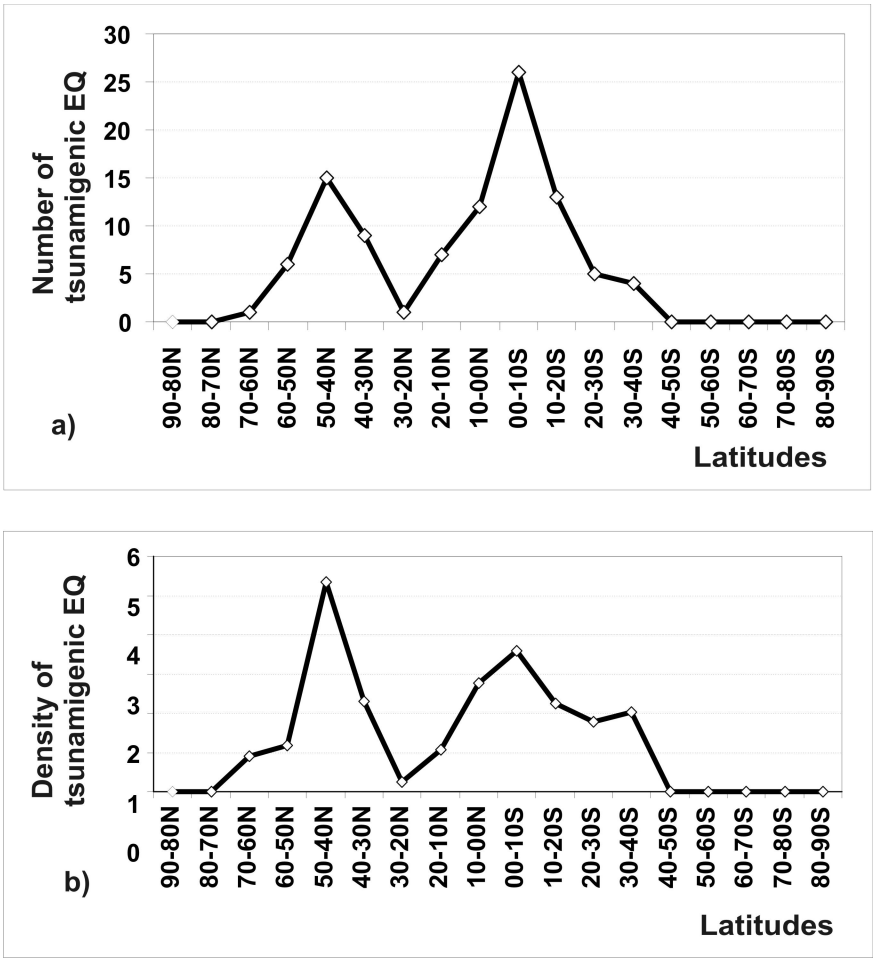

Figure 3. Latitudinal distribution of the TEQ number - (a) and the distribution of the TEQ density - (b).

The latitudinal distribution of the TEQ density is presented in Figure 3a. Basically, the distribution in Figure 3b is similar to the distribution in Figure 3a. However, the maximum in the Northern Hemisphere is marked sharper, and in the Southern hemisphere maximum in the 0° - 10°S splits into two peaks: 0° - 10°S and 30° - 40°S. The second maximum in the graph is less pronounced.

Boundaries of lithospheric plates in the northern hemisphere at latitudes 50° - 35°N and in the southern hemisphere at latitudes 10° - 40°S are located close to the meridian direction, and plate boundaries at latitudes 10°N - 20°S are mostly located in latitudinal direction. Accordingly, the total length of the plate boundaries in latitudinal belt l0° -10°S is from 2 to 3 times more than in latitudes

40° - 50°N and 30° - 20°S, which reduces the density of the TEQ in latitudes 10°S - 10°N. That is why the maximum in the Southern Hemisphere (0° -10°S) becomes not so sharp after normalization.

Figure 1 shows the location of the TEQ epicenters on the map of the World Ocean. It is easy to note that the main TEQ occur in the Pacific region. It is possible to confidently identify spatial clusters, which are located at latitudes 55° -35°N in the western part of the northern hemisphere, at latitudes 20° -40°S in the eastern part of the southern hemisphere; and events in the latitudes 10°N - 20°S which are located in both the western and eastern parts of the Pacific.

The distribution of the strong EQ number with M≥7.5 prepared on the basis of the working catalog CSEQ is presented in Figure 4. Also, clearly distinguished in this distribution are two maxima at latitudes 40° - 30°N and 0° - 20°S, a local minimum in the vicinity of 20° - 30°N and practically zero values on the polar caps and in the high latitudes. Thus the latitudinal distributions of the EQ number and TEQ number (Figure 3a and Figure 4) may be considered as being similar.

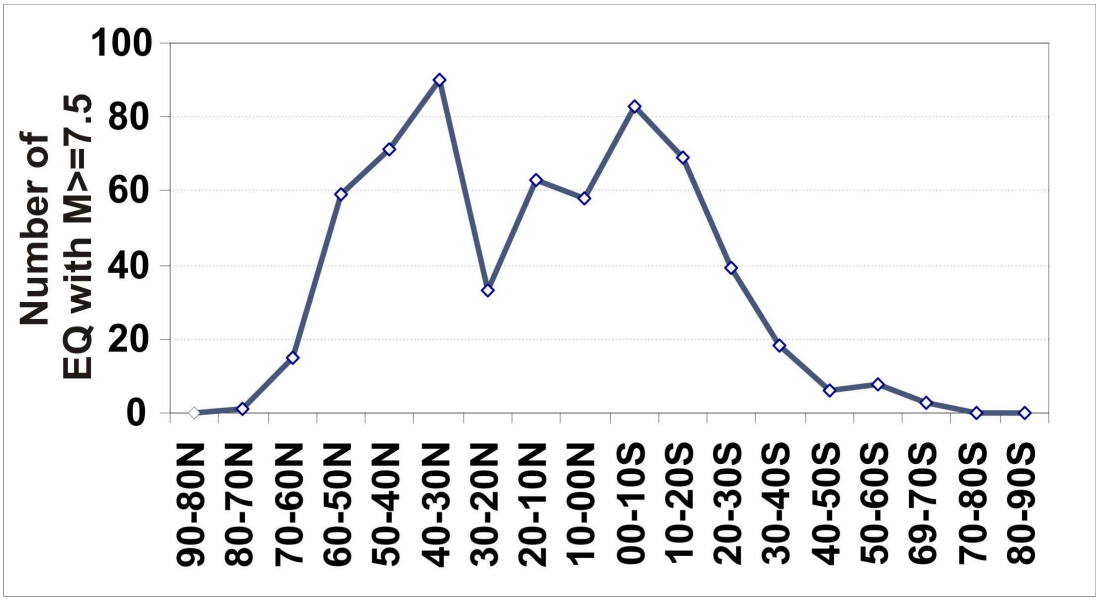

Figure 4. The distribution of the EQ number by latitude (621 events with M≥7.5). The period of observation is 123 years (from 1890 up to date).

Next, we considered the latitudinal distribution of the energy released from the TEQ (Figure 5a) and energy density (Figure 5b).

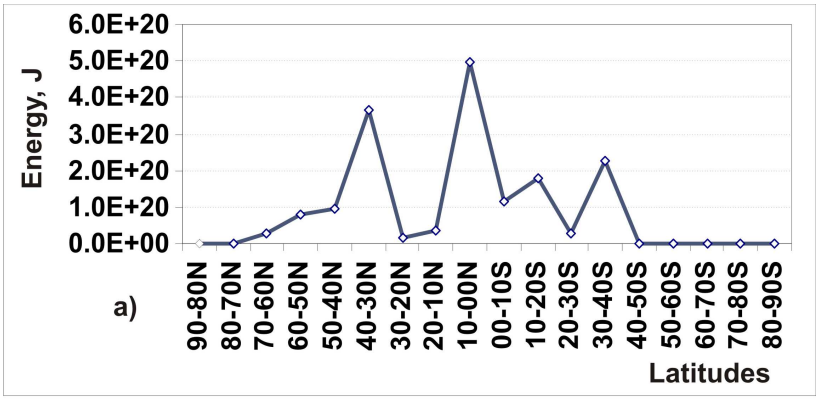

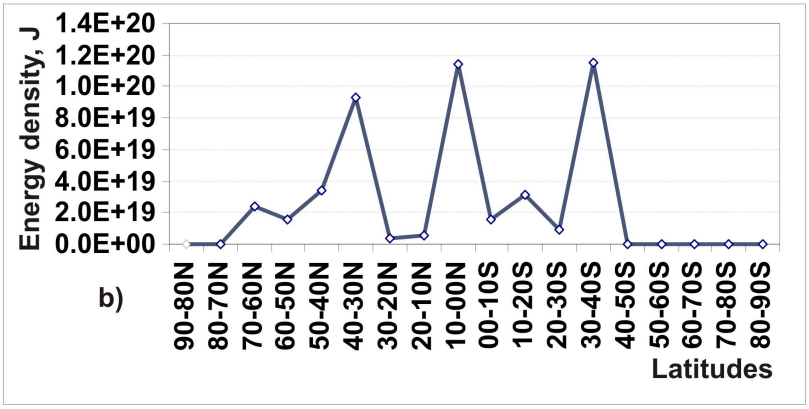

Figure 5. Latitudinal distribution of the energy released by tsunamigenic EQ – a) and the distribution of the energy density – b).

The energy released by TEQ in the latitude interval 70°N -40°S varies in range from $2.5*10^{19}$ to $5*10^{20}$, but for the latitudes 90° - 80°N and 40° - 90°S it is equal to 0.

Furthermore, we see a distribution with three clearly distinguished local maxima: at 40° - 30°N, 10° -0°N and at 30° - 40°S; local minima between them and almost zero values of energy (and energy density) on the polar caps and in the high latitudes. Peaks at latitudes 40° - 30°N and 30° - 40°S for the energy density (Figure 5b) are sharper than in Figure 5a (for released energy) as well as in Figure 3a and 3b (for the number of events and their density). About 65.8% of the total energy is released in three latitudinal belts, corresponding to the local maxima (from 18). And about 22% of the energy is released in the latitudinal belt 40° - 30°N, at latitudes 10° - 00°N the energy released amounts to 29.9%, and at latitudes 30° - 40°S to 13.7%.

The energy distributions of the TEQ presented above differ significantly from the latitudinal distributions energy density of earthquakes (Figure 6b) which have a pronounced bimodal shape with two maxima at latitudes 30° - 40°N and 20° -30°S (Sasorova et al. 2013). The distributions in Figure 6 were obtained on the basis of International Seismological Catalogue: (ISC) for more than 200000 events with M>=4.0 (data from 1964 up to date).

Both plots have a distinctly bimodal shape and location of peaks of seismic activity, being the same in the Northern and in the Southern hemispheres. Figure 6 was adopted from the work of Sasorova (Sasorova et al. 2013).

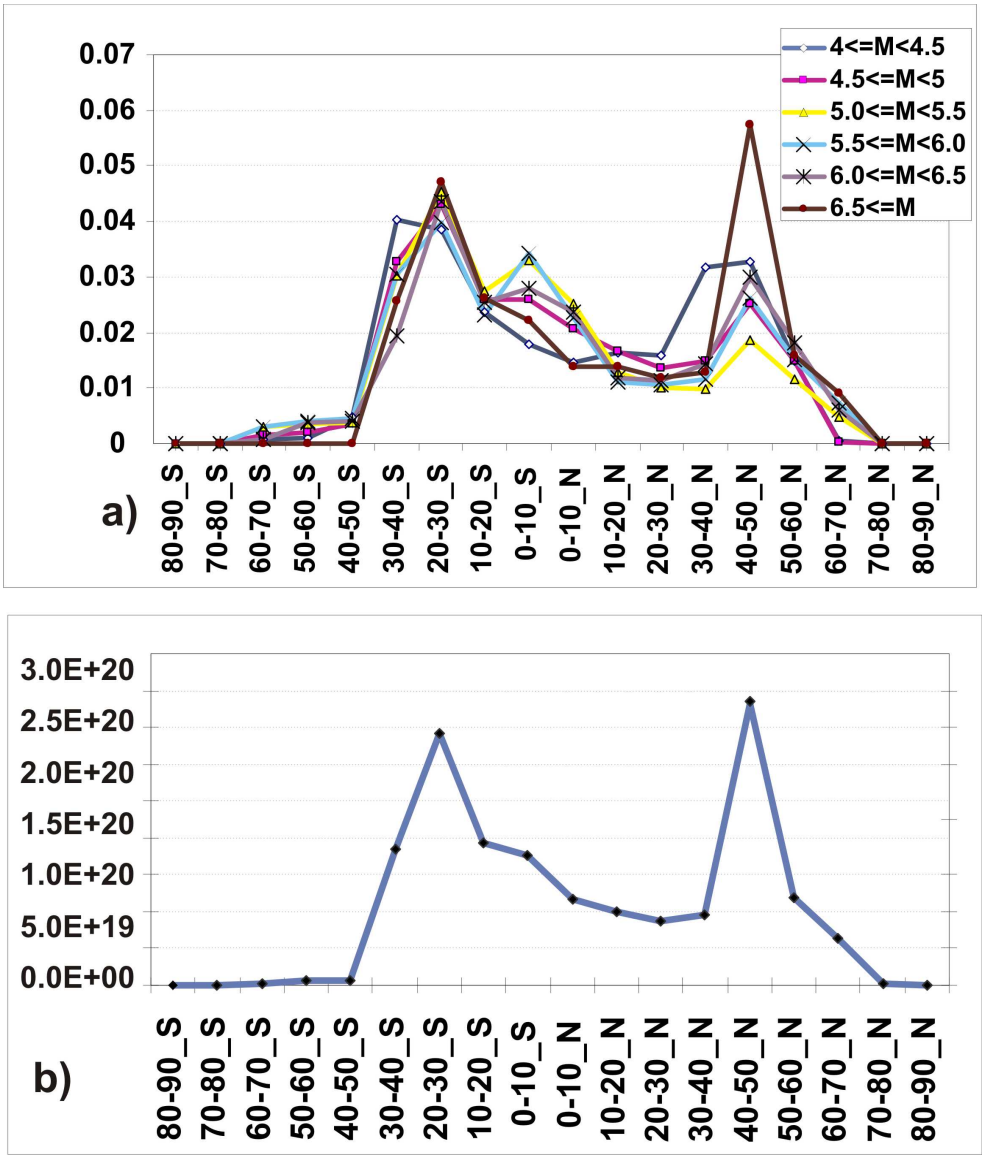

Figure 6. Distributions of the relative seismic event density by latitudes for 6 magnitude ranges – a) and the distribution of the energy density by latitudes – b).

4. THE TEMPORAL DISTRIBUTIONS OF THE TSUNAMIGENIC EQ EPICENTERS

The distributions of the TEQ density per five-year interval are shown in Figure 7: a) - for the whole Earth, b) - for the Northern Hemisphere and c) - for the Southern Hemisphere. The vertical

axes scale kept constant for all three fragments. The horizontal axes of all fragments are indicated upper limits of each five-year interval.

In Figure 7, we can observe the periodic increase and decrease of the event density in time, and the noticeable asymmetry of the increasing and decreasing of the activity TEQ for the Northern Hemisphere and for the Southern Hemisphere.

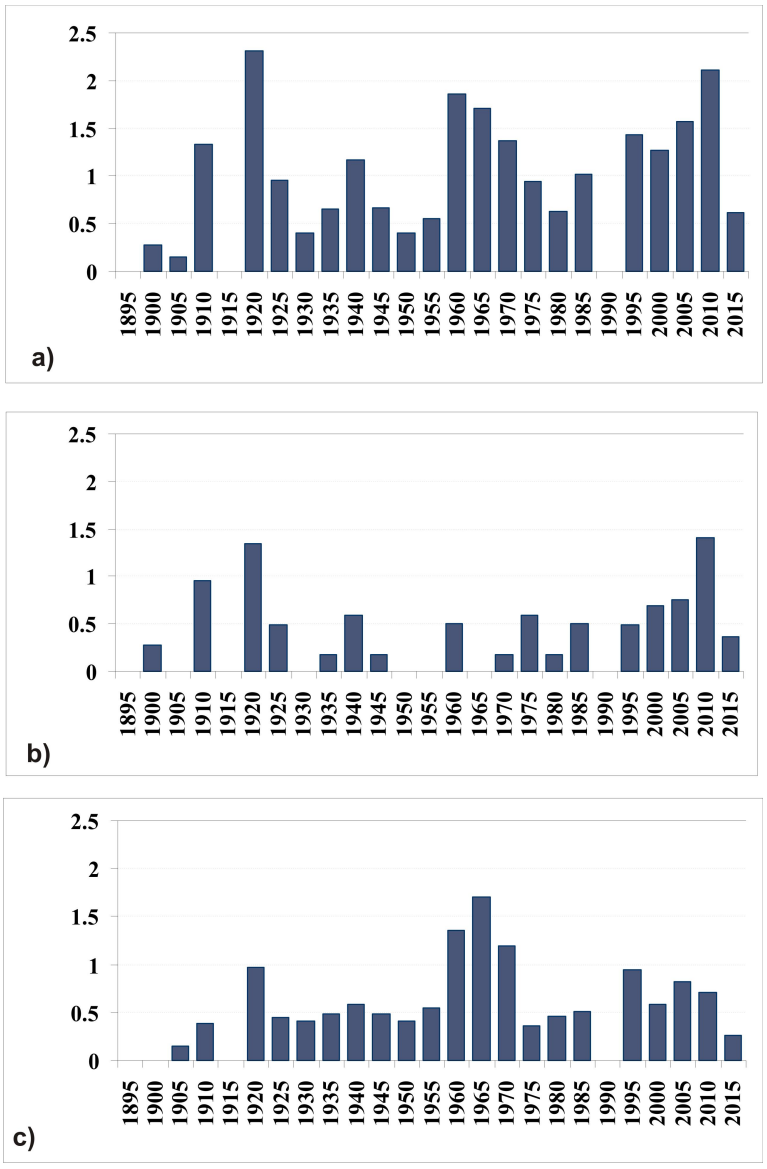

Figure 7. The distributions of the TEQ density per five-year interval: a) - for the whole Earth, b) - for the Northern Hemisphere and c) - for the Southern Hemisphere. The vertical axes are density of the TEQ. The labels on the horizontal axes correspond to upper limit of each five-year interval.

The distributions of the energy density released by TEQ per five-year interval are shown in Figure 8: a) - for the whole Earth, b) - for the Northern Hemisphere and c) - for the Southern Hemisphere.

The most powerful TEQ's occurred at the beginning of the 21st century. They occur in both the Northern and Southern Hemispheres, but in different five-year intervals.

Weaker peaks of the tsunami activity (by value of the released energy) occurred at the beginning of the 20th century and the middle of it (1950-1965). Also, detected was the periodicity of occurrence of the TEQ within the considered time period.

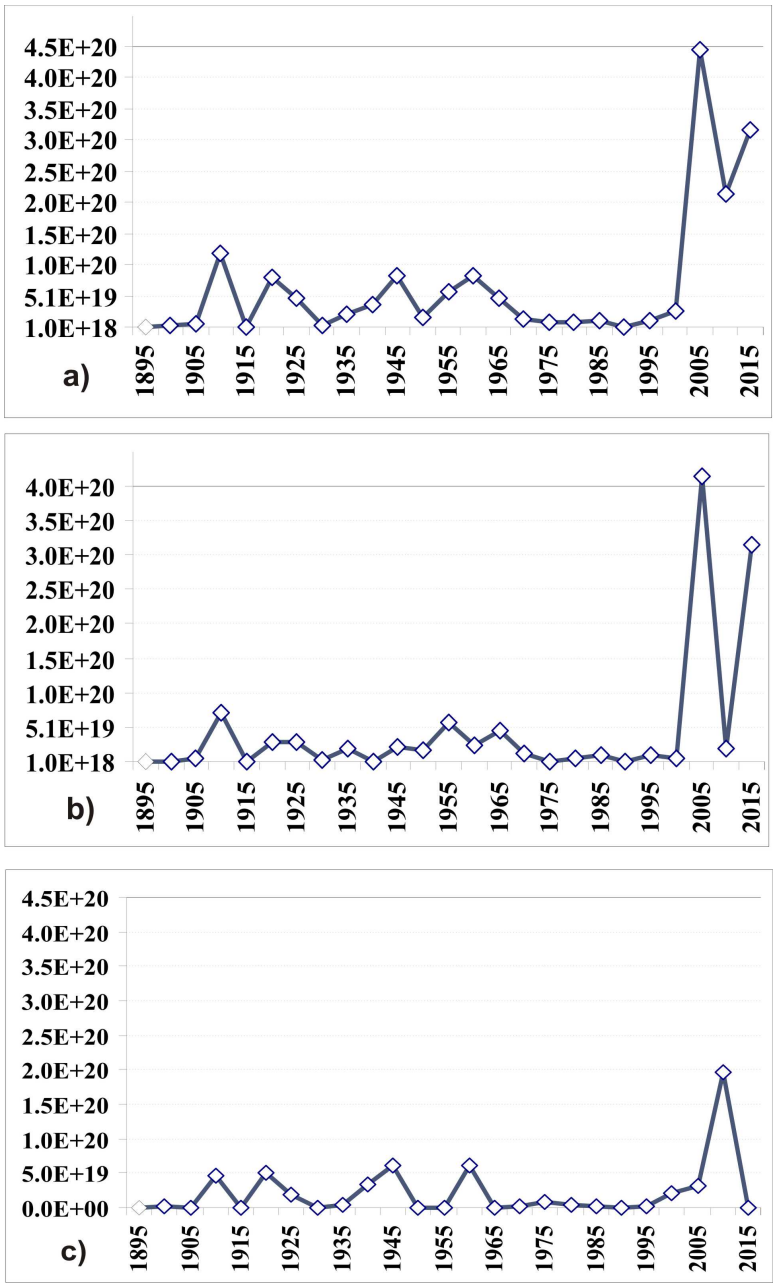

Figure 8. The distributions of the energy density per five-year interval: a) - for the whole Earth, b) - for the Northern Hemisphere and c) - for the Southern Hemisphere. The vertical axes are energy density. The labels on the horizontal axes correspond to upper limit of each five-year interval.

The increase of the TEQ activity appears sequentially in the Northern Hemisphere, and then in the Southern Hemisphere (and vice versa) as shown in Figure 9. The vertical axis indicates the total amount of energy released from these earthquakes. That part of the energy that released in the Northern Hemisphere is shown in blue, and that part of the energy which falls on the Southern Hemisphere is shown in red.

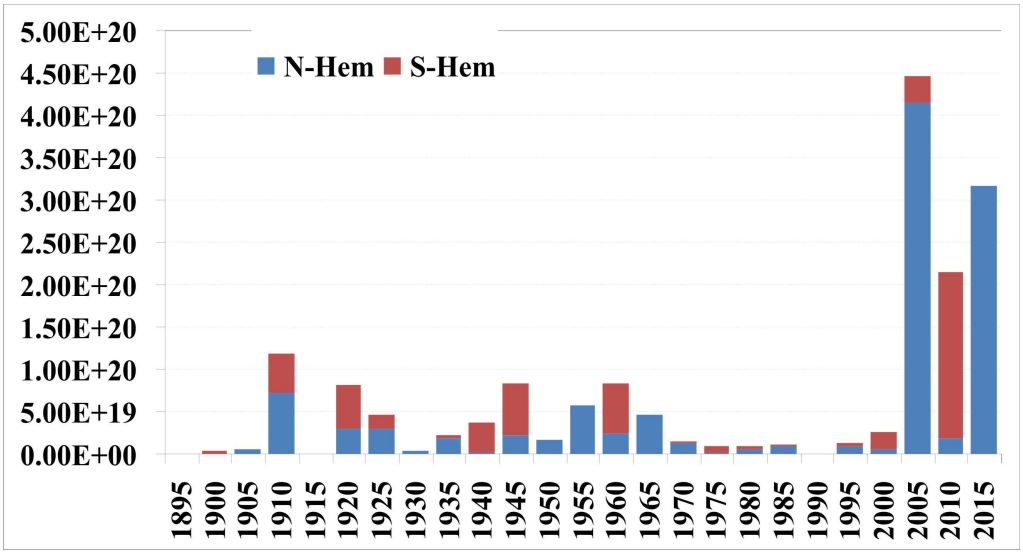

Figure 9. The total energy density distribution for the two hemispheres (red color is the part of the energy released in the Southern Hemisphere, and the blue color is the energy released in the Northern Hemisphere).

For example, the time intervals 1940, 1945 are marked generally in red (events in the Southern Hemisphere), but two following intervals (1950, 1955) are marked as blue (events in the Northern Hemisphere). Let us also consider three more powerful TEQ in the beginning of the 21 century: Indonesian Tsunami of 26.12.2004 (Northern Hemisphere), the Chilean Tsunami of 27.02.2010 (Southern Hemisphere), and subsequently, the Tohoku Tsunami of 11.03.211 (Northern Hemisphere). This feature of the sequential occurrences of strong earthquakes in different hemispheres was noted earlier in (Levin and Sasorova 2005, Sasorova et al. 2006), and for tsunamigenic earthquakes in other works (Levin and Sasorova 2002, Sassorova and Levin 2004).

Subsequently, let us compare the temporal distributions of the EQ number (with M>=7.5) in Figure 10 and the temporal distributions of the TEQ number in Figure 7. Noteworthy in Figure 10 is the observed pronounced increase and decay of seismic activity within a period about 30 years. This periodicity for the TEQ (Figure 7) is expressly much weaker.

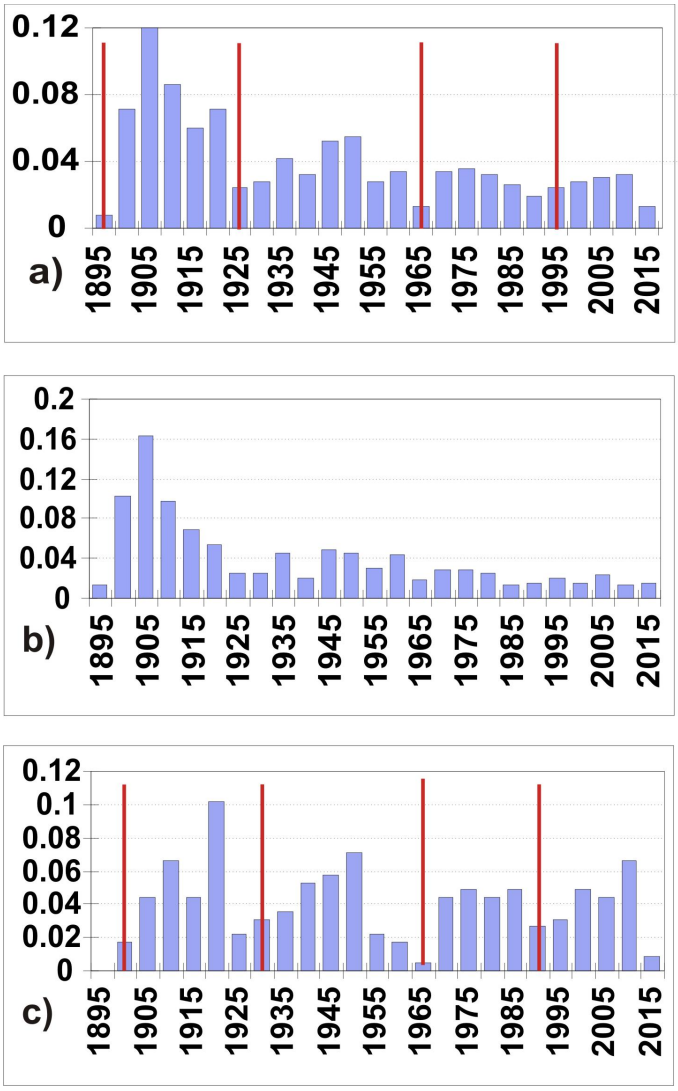

Figure10. The distributions of the relative number of the EQ with M≥7.5 per five-year interval: a) - for the whole Earth, b) - for the Northern Hemisphere and c) - for the Southern Hemisphere. The labels on the horizontal axes correspond to upper limit of each five-year interval

Subsequently we compared the temporal distributions of the energy released by EQ (with M>=7.5) in the Figure 11 and the temporal distributions energy released by the TEQ (Figure 8.)

The peaks of released energy in Figure 11 are observed in the early 20th and 21st centuries in all three fragments. The peaks of energy at the beginning of the 21st-century were generated due to a series of megaearthqakes EQ. The maxima of the energy released at the beginning of the 20-century can be explained, because of the fact that in this five-year intervals several EQ with M≥8.0 occurred(from 6 to 10 events per two year period). Also, it can be observed that two local maxima occurred in the Northern Hemisphere for the periods 1930 - 1950 and from 1950 – 1970; and two local maxima in the Southern Hemisphere: for the periods 1935 – 1955, and 1970 – 1990.

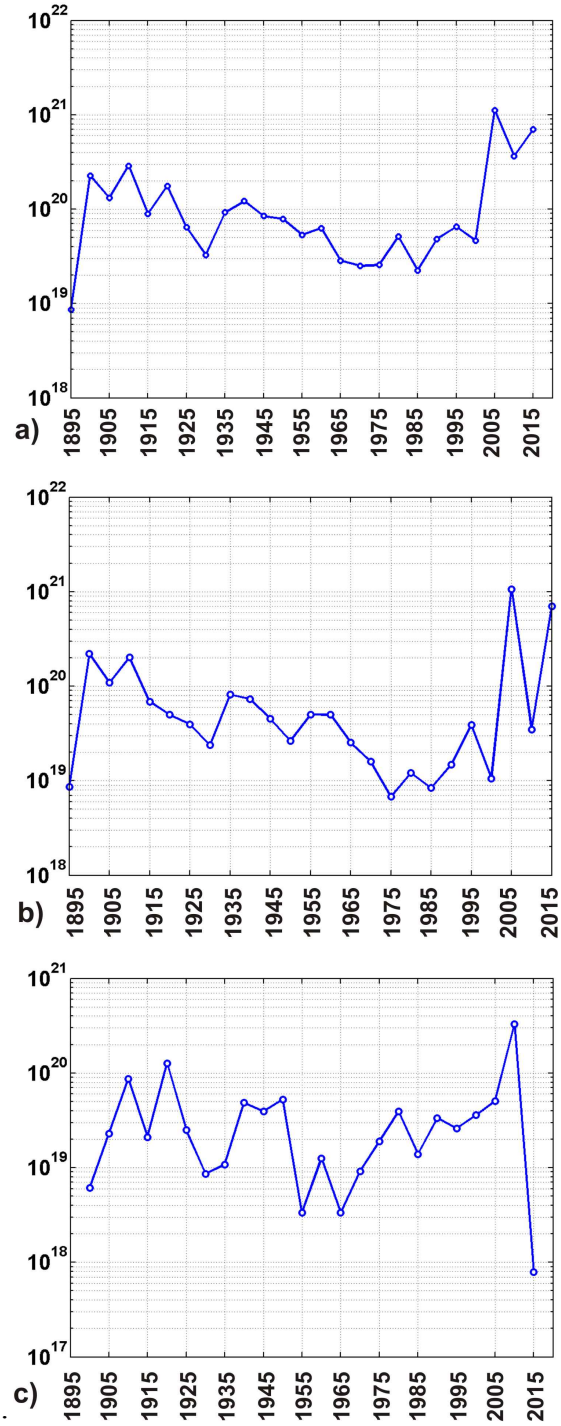

Figure 11. The temporal distributions of the energy density released by strong EQ with M≥7.5 per five-year interval for: a) - for the whole Earth, b) - for the Northern Hemisphere and c) - for the Southern Hemisphere. The vertical axes are energy density in J (logarithmic scale). The labels on the horizontal axes correspond to upper limit of each five-year interval.

5. SPATIAL-TEMPORAL DISTRIBUTIONS OF THE TEQ DENSITY AND RELEASED ENERGY

In the previous sections we discussed separately the latitudinal and temporal distributions of both density of the number of TEQ and the density of energy released from these events. However, the most complete picture gives two-dimensional, space–time, distribution of events. This representation technique of the distributions of seismic activity was used previously by the authors (Levin and Sasorova 2010, Sasorova et al. 2013).

The two-dimensional distribution of the TEQ density (Figure 12) shows that this representation identifies areas in which for more than a hundred years any tsunamigenic EQ (polar caps and high latitudes) did not occur. However, the situation is different for the Southern hemisphere since it comprises a much more extended zone, extending from 40°S up to the South Pole. The same holds true for the Northern hemisphere since this area starts from 70°N. It is interesting to note that the area with very weak tsunami EQ activity (practically zero-order) was observed in the latitude belt 30° - 20°N.

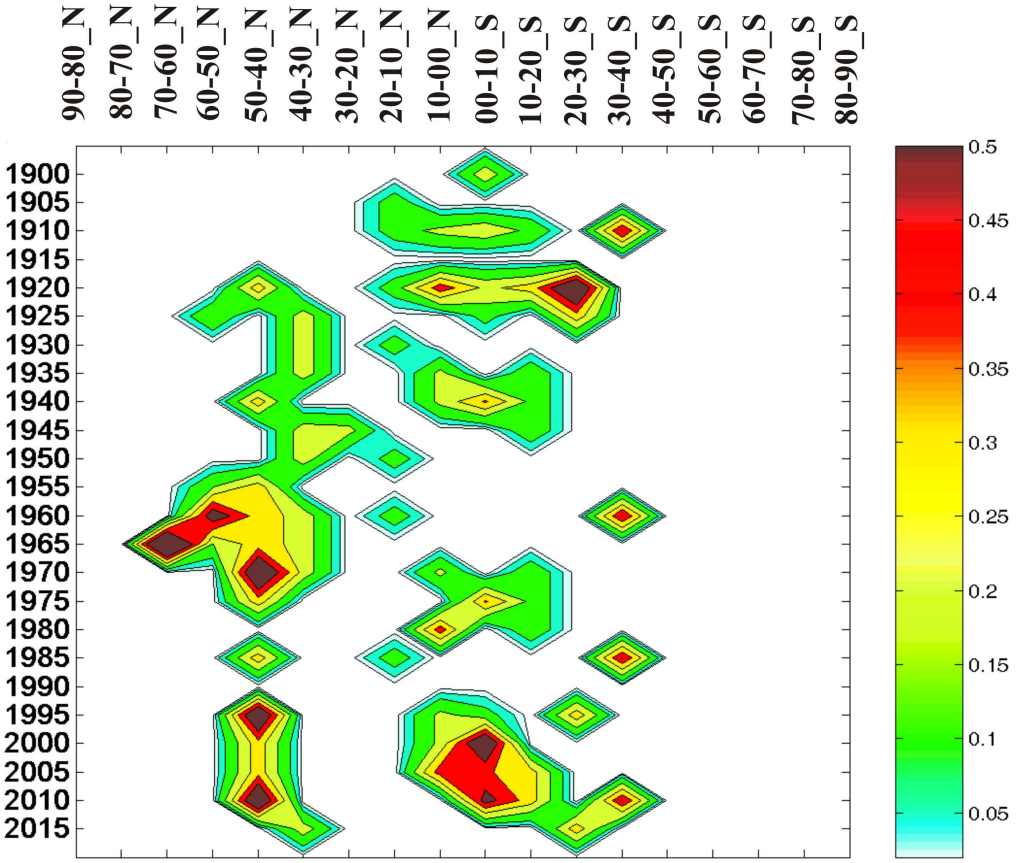

Figure12. Two-dimensional distribution of the TEQ density by latitude and time from 1985 to 2013. The labels on the vertical axis correspond to upper limit of each five-year interval along the horizontal axis - latitudinal belts. The color scale on the right side of the figure corresponds to the density of events.

The occurrence periodicity of tsunamigenic earthquakes is clearly shown in Figure 12. The periods of TEQ activity intensification are not coinciding at different latitudinal zones. In the Northern Hemisphere peaks of activity of several large events can be observed at a comparatively short time intervals. Specifically, such peaks of activity occurred in the middle of the 20th century from 1955 to 1975, then after a 20-year interruption, by subsequent events from 1990 to 2010. There are also two, less powerful clusters in the time intervals from 1915 to 1920 and from 1980 -1985.

In the equatorial region peaks tsunami activity are observed at intervals of 25 years (in the first half of the 20th century), then at intervals of 30-40 years (mid-century), and again at intervals of 25 years to the end of the 20th century. In the Southern Hemisphere almost identical peaks of the tsunami activity are observed at intervals of 50 years in the first half of the 20th century, thereafter at intervals of 25 years from 1960 up to date.

Figure 13 shows a two-dimensional distribution of the energy density released by the TEQ. This distribution is generally identical to the distribution in Figure 12. The color scale on the right side of the figure gives the value of the released energy $E = 10^N$ in J. The two-dimensional distribution of the energy density almost coincides with the two-dimensional distribution of the density events.

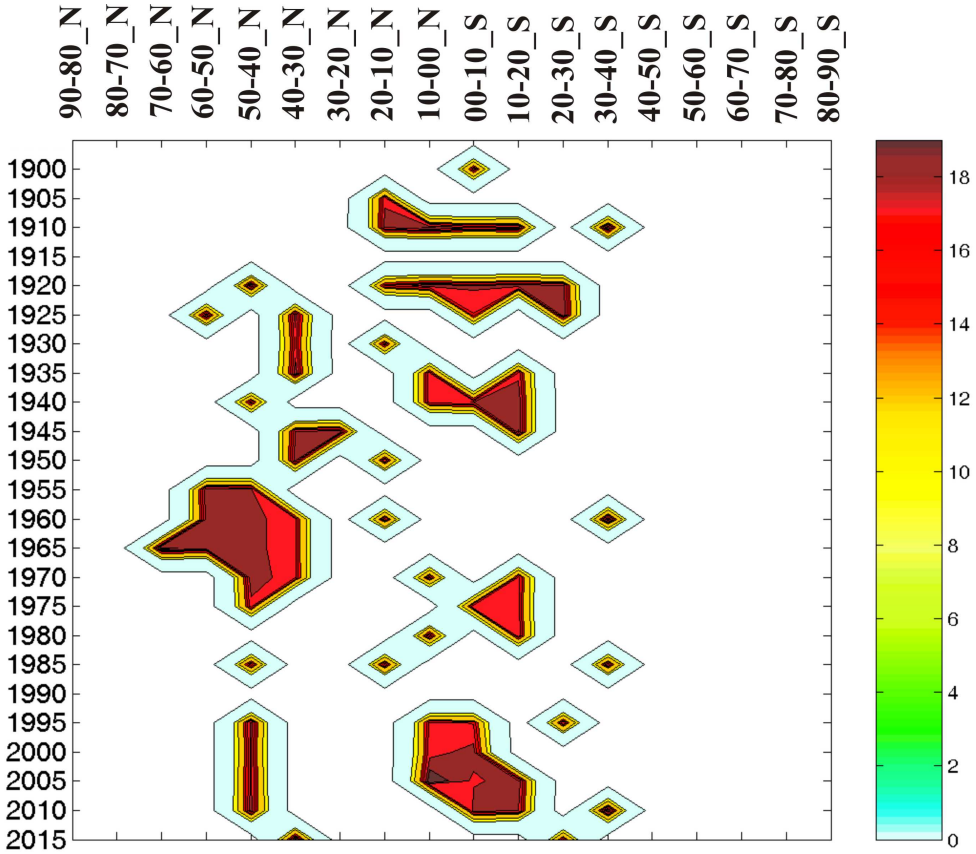

Figure 13. Two-dimensional distribution (by latitude and by time) of the energy density for the TEQ from 1985 to 2013. Legends of all axes are the same as in Figure 12.

6. PECULIARITIES OF THE DISTRIBUTION OF THE TEQ SOURCES IN THE PACIFIC REGIONS

Let us now consider the spatial-temporal distributions of the TEQ sources in the following sub regions: Kuril-Kamchatka, Japan area, South America, Central America and the equatorial zones, as well as the periodicity of manifestation of tsunamigenic earthquakes in the regional distributions.

The spatial-temporal distribution of the TEQ epicenters for the Kuril-Kamchatka zone is shown in Figure 14. It may be noted that no tsunamigenic earthquakes are observed in the latitude belt from 47°N to 51°N, in the time interval from 1900 to 2013. However, there is a coincidence in the appearance of the TEQ in Kamchatka and the Kuril Islands in certain time intervals from1915 to 1920 and from 1950 to 1960, and in the periodicity of tsunami occurrence with periods of 20 to 35 years.

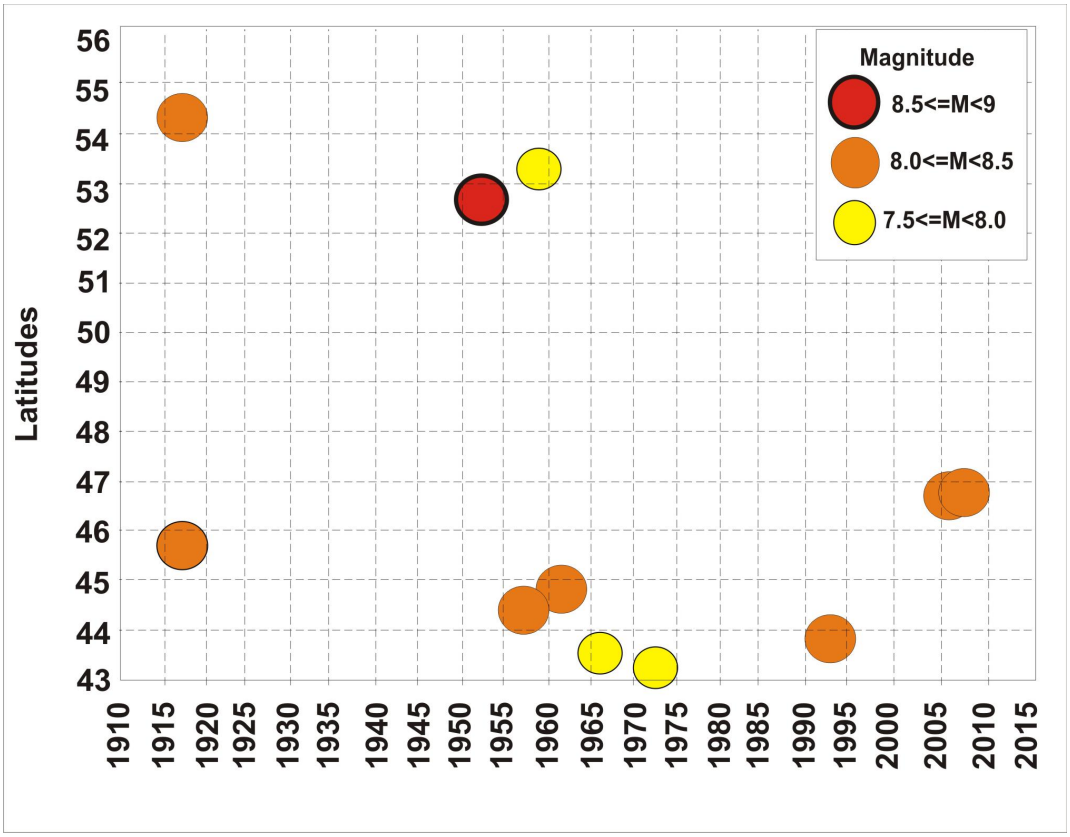

Figure 14. The two dimensional distribution of the TEQ in the Kuril-Kamchatka region (by latitudes and by five-year interval). The vertical axis represents latitudes of the TEQ epicenter. The labels on the horizontal axis correspond to the upper limit of each five-year interval. The magnitude legend is in upper-right corner.

The spatial-temporal distribution of the TEQ epicenters for the Japan zone is presented in two fragment of Figure15 (15a – the Pacific part of Japan and 15b - the Japan sea).

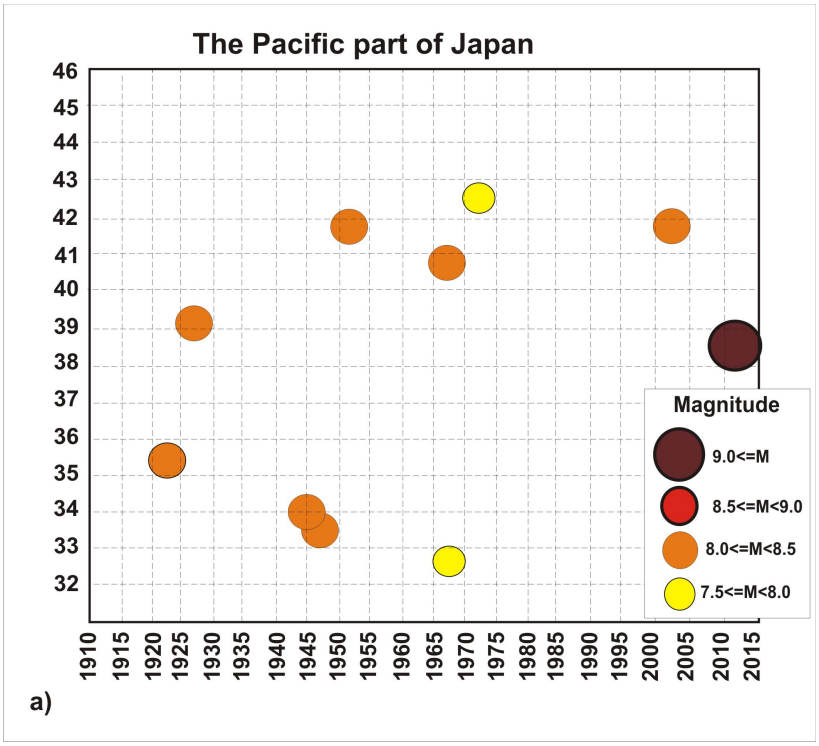

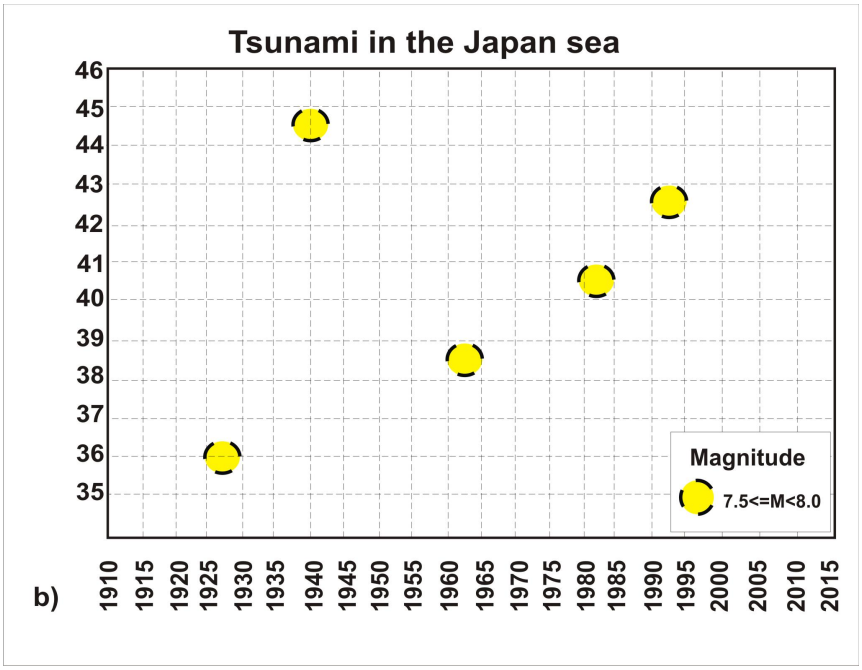

Figure 15. The two-dimensional distributions of the TEQ (per latitudes and five-year interval): a) - in the Pacific part of Japan, b) in the Sea of Japan. The vertical axes are the latitudes of the TEQ epicenter. The labels on the horizontal axes correspond to the upper limit of each five-year interval. The magnitude legend is in bottom-right corner of each plot.

The latitudinal belt from 34°N to 40°N in Figure 15a may be discriminated, where from 1930 to 2010 strong tsunamigenic earthquake epicenters were not observed. The periodicity of the intensifying tsunami activity with periods 20 - 25 years may be marked. In the latitude belt 38°N - 45°N (Figure 15b, Sea of Japan) a migration of the TEQ epicenters is noted from south to north in the period (1960-1995) with a periodicity of about 20 years. All epicenters of tsunamigenic earthquakes in this latitude belt, locate almost on the same longitude (139.09°E to 139.53°E).

The spatio-temporal distribution of the TEQ epicenters in South America (Pacific Coast) is shown in Figure 16.

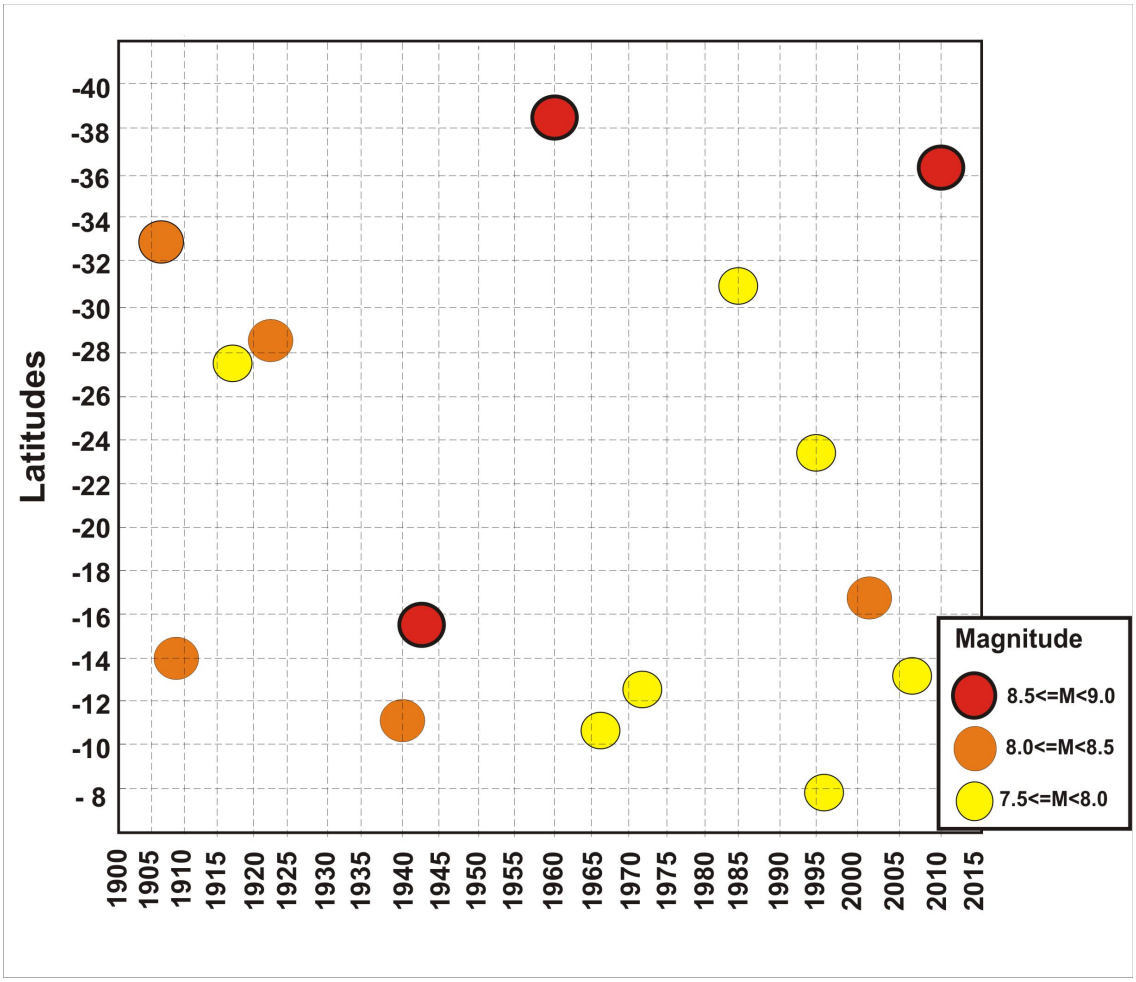

Figure 16. The two-dimensional distributions of the TEQ (by latitudes and by five-year interval). The vertical axis shows the latitudes of the TEQ epicenters. The labels on the horizontal axis correspond to the upper limit of each five-year interval. The magnitude legend is in bottom-right corner of the plot.

An analysis of figure 16 allows us to mark:

- the existence of two latitudinal belts from 8°S to 18°S and from 26°S to 40°S, where almost all the epicenters of the TEQ are located.
- the latitude interval which display weak tsunami activity ranges from 18°S - 26°S.

The frequencies of occurrence of tsunamigenic earthquakes in active zones are different and range from 25-30 years for zone 8°S - 18°S and from 45-50 years for the belt 26°S - 40°S. These periodicities may be observed before where we analyze Fig. 12 and Fig. 13. Periods of activation in the zone of 26°S - 40°S correspond mainly to periods of activity decrease in the zone of 8°S - 18°S.

The spatio-temporal distribution of TEQ epicenters for Central America (Pacific Coast and Caribbean region) is given in Figure 17.

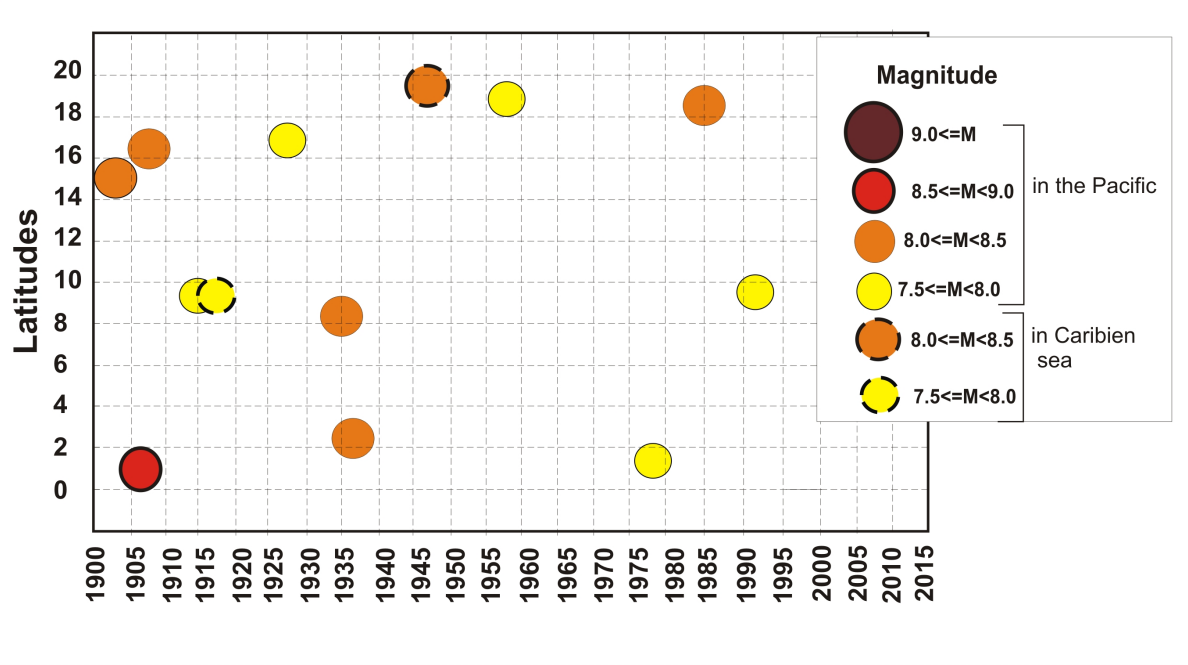

Figure 17. The two-dimensional distributions of the TEQ (per latitudes and per five-year interval). The vertical axis is the latitudes of the TEQ epicenter. The label on the horizontal axes corresponds to upper limit of each five-year interval. Legend for magnitude is in upper-right corner of the plot.

The spatial differentiation of the location of the TEQ epicenters in this figure is not expressed adequately. However a periodicity of 30-35 years for the TEQ sources located in the Pacific Ocean can be seen. After 1991, no significant tsunamis in this region were observed.

The spatio-temporal distribution of TEQ epicenters for the subequatorial region of the Pacific is given in Figure 18.

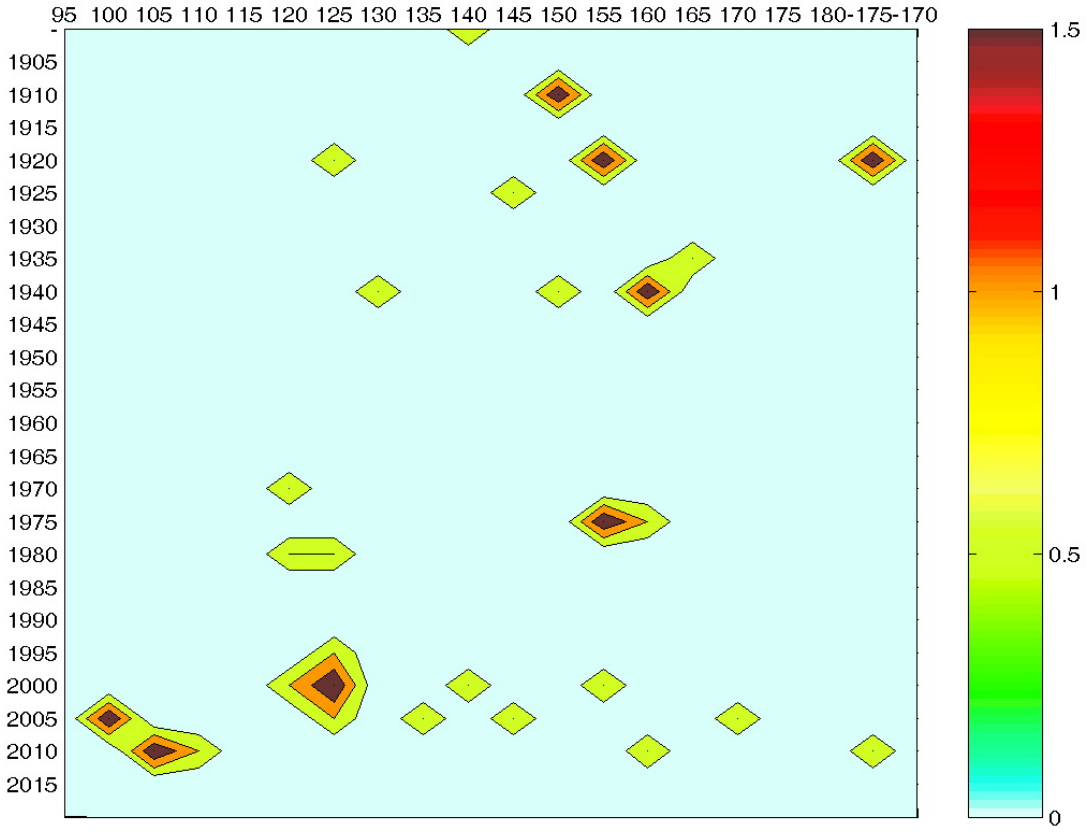

Figure 18. The two-dimensional distributions of the TEQ (by longitudes and by five-year interval). The horizontal axis is the longitudes. The labels on the vertical axis correspond to upper limit of each five-year interval. The color scale of the TEQ density is in the right corner.

This region (see Figure 1) has an extended longitudinal area with the length of the boundaries of the lithospheric plates being about 6600 km. Therefore, the two-dimensional distribution is represented here: longitude - time (in contrast to the previous figures with distributions of latitude-time).

In the region ranging from longitude 95°E to 120°E no events were observed from 1900 to 1965. Also, reduced tsunami activity is shown from 1940 to 1970. An increase in activity in the zones ranging from 115°E to 120°E and from 150°E -155°E, occurred from 1970 to 1985.

After the events of 02.07.1996 and of 29.11.1998, the tsunami activity increased throughout the equatorial zone until 2004, when the catastrophic Indonesian tsunami 26.12.2004 occurred, followed by a series of events (6 tsunamigenic earthquakes). The series contain four events with epicenters located in a relatively small longitudinal zone from 97°E to 107°E (two of the four events had M = 8.5).

The energy distributions for the selected regions are not presented here because the maximum of the distribution of the energy released by the TEQ, corresponds to the location of the strongest events

in each region. For example, these maxima in time and space correspond to the following catastrophic events: for the Kuril-Kamchatka zone - Kamchatka TEQ (4.11.1952) and two Simushir TEQ (2006 and 2007); for Japan -a catastrophic earthquake in Tohoku (11.03.2011); and for the equatorial zone - Indonesian TEQ (26.12.2004).

7. DISCUSSION AND CONCLUSIONS

First of all, we considered the statistical characteristics of the TEQ, which were identified taking into account the magnitude and geographical parameters of their distributions. The resulting working catalogs (CTEQ and CSEQ) allowed us to answer the question: what part of the strong EQ generates a tsunami if the magnitude threshold of a strong EQ varies from: 7.5, to 8.0, to 8.5. These data were calculated and are presented in Table 1 below.

Table 1. A comparison of the number of strong earthquakes with the number of tsunamigenic earthquakes of the same magnitude.

	Events with M≥7.5		
	The whole Earth	Northern Hemisphere	Southern Hemisphere
Total number of the EQ	621	393	228
Number of the TEQ, with I>=1	100 (16%)	51(13%)	49 (21%)
	Events with M≥8.0		
Total number of the EQ	175	119	56
Number of the TEQ, with I>=1	47 (30%)	28 (24%)	19 (340%)
	Events with M≥8.5		
Total number of the EQ	9	5	4
Number of the TEQ, with I>=1	9 (100%)	5 (100%)	4(100%)

It is shown that the average number of the tsunamigenic earthquakes is equal to 16% for events with M≥7.5 and near 29% - for events with M≥8.0. The relative number of the TEQ in the Northern Hemisphere is more than in the Southern Hemisphere for all magnitude ranges.

However, all the catastrophic EQ (with M≥8.5) result to tsunami generation. The epicenters of these events are located in the Pacific (4 - in South America, 3 - in the northern part of the equatorial zone, 1 - on Kamchatka, 1 - in Japan). It should be mentioned that these features of the distributions the TEQ were reflected in previous studies [Levin and Sasorova 2002, Levin and Sasorova 2013].

Comparison of the number of the strong EQ with the number of tsunamigenic earthquakes and of the released energy to the five regions of the Pacific (for three magnitude ranges). These data were calculated and are presented in Table 2 below.

Table 2. A comparison of the number of strong earthquakes with the number of tsunamigenic earthquakes of the same magnitude for five regions.

		Events with M≥7.5			
	Kurile-Kamchatka zone	Japan	The near-equatorial belt	The South America	The Central America
Latitudes Longitudes of the regions	43°N-55°N 144°E-165°E	32°N-46°N 130°E-144.5°E	6.3°N-19.5°S 95°E-168°W	8.5°S-40°S 85°W-65°W	20°N-0°N 110°W-60°W
Total EQ number	43	64	124	60	67
Number of the TEQ, with I>=1.	11 (26%)	14(22%)	38 (31%)	16 (26%)	12 (18%)
		Released energy, J			
Total sum	1.73E ± 20	8.71E ± 20	1.42E ± 21	4.96E ± 20	2.8E ± 20
Released by the TEQ with I≥1	1.16E ± 20 (67%)	4.00E ± 20 (46%)	5.94E ± 20 (42%)	3.8E ± 20 (76%)	1.0E ± 20 (38%)

The relative number of events with M≥7.5 generated a tsunami and the range of magnitudes averaged over all regions increased to 24.6% (compared with 16% of the tab. 1). This may be explained by the fact that numerous events in mainland Asia are not located in Pacific regions, so the total number of EQ decreased (from 621 to 595).

However, for all regions that were examined, the amount of energy released by the TEQ averaged more than 50% (53.8%), and this ratio varies from one region to another. So in South America and the Kuril-Kamchatka zones the energy released by the TEQ is equal to 76% and 67% of the total energy, respectively, with the catastrophic EQ contributing most of the energy.

At the present time the detection of tsunami waves in the open ocean is a solvable problem. However, when the tsunami source is close to the coast, it is very difficult to issue a local tsunami warning within a 15 to 20 minutes before the first of the tsunami waves strikes, so the magnitude-geographical principle remains the dominant factor for evaluation. It is assumed that tectonic tsunamis are generated by earthquakes for which $M \geq M_{tr}$ and that there exists a dependence of the tsunami waves' intensity (I) on the EQ magnitude: I=f (M). The M_{tr} is the threshold value, which is chosen separately for each region.

Attention to another study (Gusiakov 2011), should be drawn, in which a detailed investigation of the intensity of the tsunami waves on the magnitude TEQ on the basis of observational data was provided – specifically for various examined observation periods (from 1900 to 2010 and from 1990 to 2010) and for different magnitude scales for the events that generated tsunami. Attempts to find a significant correlation between the magnitude of the tsunamigenic earthquake and the intensity of the tsunami waves were not successful up to now.

A scatter chart for the observation period from 1900 to 2010 shows that for events with $M \geq 7.5$ and $I \geq 1$ the regression equation with an acceptable value of R^2 (the value of the reliability of the approximation) was not possible. Data in this range is almost uniformly distributed within a rectangular window (Figure 19).

The R^2 values we recalculated on scatter charts for linear regression on the basis of data presented in the catalogs, varied from 0.11 to 0.25, which does not suggest the presence of significant dependence I=f (M). Using the quadratic regression dependence did not lead to a noticeable improvement in the value R^2. However, the lack of sufficiently reliable functional dependence I = f (M) leads to the appearance of false tsunami warnings.

The above listed facts suggest:

- a weak correlation between the intensity of the tsunami and the earthquake magnitude;
- a sharp decline in the share of the TEQ (16%) if the threshold of the EQ magnitude is decreased to $M \geq 7.5$;
- a significant difference in the latitudinal distributions of energy for a strong EQ and TEQ;
- detection of periodicities of the tsunami occurrence in space and time;

Apparently, these lead to the conclusion that the TEQ, have a specific properties that arise in their sources, thus requiring additional research in determining the characteristics of such sources.

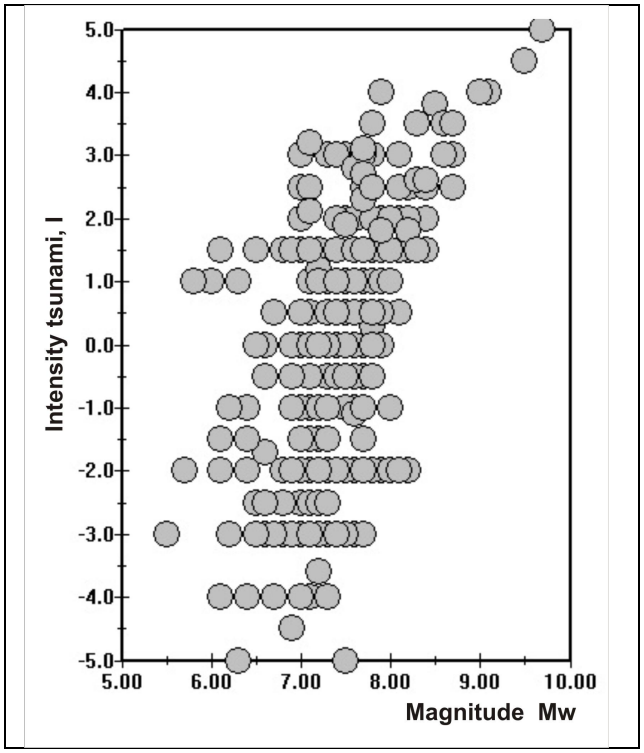

Figure 19. Scatter chart for 360 tsunamigenic events in the world's oceans from 1900 to 2010 (with M>5.0, and I>-5.0). Events are marked by circles gray. The intensity of the tsunami on the scale defined Soloviev-Imamura. Figure was adapted from (Gusiakov, 2011).

The focal sources for most earthquakes (98%) that generated the tsunamis shown in the CTEQ catalog had a depth of H≤60 km. In the working directory (before preprocessing) only four events did not satisfy the above condition of focal depth (for two events the earthquake focal depth was not been determined, one having H = 80 km, and the other one having H = 230 km). All these events belong to the early instrumental period (until 1923), where there was a large error in the determination of earthquake focal depth.

The number of events with H <= 60 km for the EQ with M> = 7.5 is equal to 86%, about 6% of the EQ has depth 60 <= H <120 km, the depth 6% of the EQ is 120 <= H <350 km, and about 2% of the EQ have depth equal to H> = 500km.

Analysis of Figures 12 and 13 indicates that occurrence and frequencies of tsunamigenic earthquakes is greatly affected by regional peculiarities. This may be caused by the fact that almost all sources of the TEQ in the western part of the Pacific are associated with the boundaries of compressed island arcs.

The minimum distance from the source to the coast (MD) for each tsunamigenic earthquake and the MOD values (average value of the MD values defined for all events in the region) were previously calculated (Sasorova et al. 2008) which also determined that 87% of the TEQ sources in the Pacific

basin were no further than 100 km from the closest shoreline, and for some regions (Kamchatka, Central America, Japan - Sea of Japan) all the epicenters of the TEQ were located within the one hundred kilometer zone and that about 68% of the total number of the TEQ were located even closer within the 50 km zone. It was shown that most of the tsunami sources in Central America were located near the coastlines. The MOD value for this Central America region is equal to 10 km, and for South America the MOD value is = 34 km.

The close proximity of the source of a potential tsunamigenic earthquake to the coast may give the impression of false tsunami warnings for such regions, since the magnitude of the event is the only criterion used in the evaluation of the potential tsunami hazard.

A statistical analysis of TEQ of tectonic origin shows that a significant part of these events occur on the continental shelf, on the shallow part of the ocean near the coast, and in regions located near island arcs and marginal seas. In such areas, a substantial amount of sediments accumulates (Lisitzin 2013). Thus, when a substantial earthquake strikes, an unstable accumulation of sediments on the continental slopes may cause a shift of large masses of sedimentary material, underwater landslides and in the generation of a catastrophic tsunami. Our study noted that after a strong tsunamigenic earthquake occurred, a second event in the same region after 0.5 - 1 year, did not generate as strong of a tsunami. This observation indicates the need for a more careful and detailed analysis of the physical parameters as the sources of the TEQ and the geological conditions of the source's development.

At the end of the last century (Burymskaja et al. 1981), it was suggested that the sources of the TEQ have a relatively low average speed of the rupture generation and the long duration of the amplification of the oscillation intensity in P-wave. This may cause the redistribution of the energy balance in the focus and gain share in the low-energy part of the spectrum.

The peculiarities of the TEQ occurrences which were indicated above, can lead to some conclusions about some of the features, which are inherent just to tsunamigenic events.

1. Catastrophic earthquakes in the ocean ($M \geq 8.5$) are almost always accompanied by a tsunami (100%), while strong earthquakes ($M \geq 7.5$) generate a tsunami in only 24% of the cases (for the Pacific region). Such a selective response to a mechanical perturbation of the ocean can be associated with a rare appearance of EQ witth a predominance of low-frequency components in the signal, generating less energy density.

2. Also noted was the zonal structure of the alternation in tsunami activity. Latitudinal zones of high activity were interchanged with zones of weak activity. The peaks of activity emerged in different times for different latitudinal zones, and the activation periods varied from 20 to 50 years.

3. Observed regularities can be the basis for constructing a model of tsunami occurrence taking into account the spatial and temporal distribution of events. A verification of the model involving algorithms and subsequent analysis of results, allow formulating new approaches to forecasting catastrophic tsunamis.

Model development of the evolution of the tsunami sources in space and time and verification (specification) models using observational data, will allow to advancement in the understanding of the causes of catastrophic tsunamis.

ACKNOWLEDGMENTS

This work was supported partly by the Russian Foundation for Basic Research (projects No. 10-05-00116a, 11-05-07016d, 12-05-10031k and 13-05-00060a). We are grateful to Mikhail Nosov, Mikhail Rodkin and Yegenio Chirkov for the creative discussions and fresh wording, and we also express many thanks to Alik Ismail-Zade for useful comments in statistic technique.

REFERENCES

Burymskaia, R.N., Levin, B.W., Soloviev, S.L. (1981) A Kinematic Criterion of Submarine Earthquake Tsunamigenity // Doklady Akademii Nauk SSSR. Vol. 261, № 6. P. 1325-1329.

Gusiakov V. K. (2011) Relationship of Tsunami Intensity to Source Earthquake Magnitude as Retrieved from Historical Data, Pure Appl. Geophys. (168) 2033–2041, DOI 10.1007/s00024-011-0286-2

Historical Tsunami Database for the World Ocean -2010, (HTDB/WLD 2010), http://tsun.sscc.ru/nh/tsunami.php

(ISC), International Seismological Catalogue: http://www.isc.ac.uk/iscbulletin/search/catalogue/.

Levin, B. W. and E. V. Sasorova. (2002) On the 6-Year Tsunami Periodicity in the Pacific. J. Izvestiya, Physics of the Solid Earth, Vol. 38, No. 12, p. 1030.

Levin B.W., Sasorova E.V. (2002) Spatial and temporal periodicity in the Pacific tsunami occurrence. 3-rd Biennial Workshop on Subduction Processes emphasizing the Kurile-Kamchatkan-Aleutian Arcs. Fairbanks, Alaska, USA, June.

Levin, B. W. and E. V. Sasorova. (2005) Detection of Nonrandom Component in the Earthquake Distribution between the Northern and the Southern Hemispheres: Observations and Modeling. Doklady Earth Sciences. Vol. 401, No 2, pp.288-291.

Levin, and E. V. Sasorova. (2010) General Regularities in the Distribution of Seismic Events on the Earth and on the Moon. Doklady Earth Sciences, **DOI:** 10.1134/S1028334X10090230, Vol. 434, Part. 1, pp. 1249–1252.

Levin B.W., Sasorova E.V. (2013) Tsunami and Great Earthquake Space-Time Periodicity: Comparative Analysis. International Tsunami Symposium. ITS2013. Gochek, Turkey; Rhodes, Greece, 25-28 September. P.31.

Lisitzin A.P. (2013) Marine Geology - 40 years of the conference. Geology of seas and oceans. Proceedings of the XX International Scientific Conference (School) of marine geology. Vol.1. Moscow, p.5-13 (in Russian).

NGDC/NOAA (2010), Historical Tsunami Database (2010), Web-version: http://www.ngdc.noaa.gov/hazard/tsu_db.shtml.

Sasorova, E.V. and B.W. Levin. (2004) Spatial and temporal periodicity in the Pacific tsunami occurrence. Submarine Landslides and Tsunamis, NATO Science Series IV, Earth and Environment Science, p.43-50, Kluver Academic Publishers.

Sasorova E.V., B.W. Levin, O.N. Emelyanova. (2006). Detection of the non-random component in the earthquake distribution between the Northern and Southern part of the Pacific: observation and modeling. Earthquake Prediction. Ed. S. Mukherjee. Brill. Leiden-Boston. P.1-8.

Sasorova E.V., Korovin M.E., Morozov V.E., and Savochkin P.V. (2008) On the Problem of Local Tsunamis and Possibilities of Their Warning. ISSN 0001-4370, Oceanology, , Vol. 48, No. 5, pp. 634–645.

Sasorova E.V., Levin B.W., and Rodkin M.V. (2013) A common feature in latitudinal dependence of different geophysical processes occurring on the rotating Earth. Adv. Geosci., 35, 15–21, doi:10.5194/adgeo-35-15-2013.USGS/NEIC http://neic.usgs.gov

ISSN 8755-6839

SCIENCE OF **TSUNAMI HAZARDS**

Journal of Tsunami Society International

Volume 34 **Number 1** **2015**

NUMERICAL SIMULATIONS OF AN EVACUATION FROM A TSUNAMI AT PARANGTRITIS BEACH IN INDONESIA

Radianta Triatmadja
Department of Civil and Environmental Engineering,
Tsunami Research Group, Research Centre for Engineering Science
Universitas Gadjah Mada, Yogyakarta, 55281, Indonesia
radiantatoo@yahoo.com

ABSTRACT

The tsunami disaster in Calang (Aceh, Indonesia) in December 2004 caused traffic jam at a bottleneck on an evacuation road that was fatal, killing most of the evacuees. This tragedy provides an invaluable lesson for evacuation planning in several other locations that are prone to tsunami events. Parangtritis is a local tourism destination that is also prone to tsunami hazard. Although the evacuation routes have been prepared and evacuation direction sign boards have been provided, a study on their capacity and suitability were required. One of the methods was employing mathematical simulations. This paper addresses the development of a mathematical model based on the Dijkstra algorithm and its application to evacuation during a tsunami at Parangtritis Beach, Indonesia. The running speeds of evacuees were derived from world athletes' running records but with significantly lower coefficients to model ordinary people. Trial runs were also carried out to calibrate the value of f that represented the ratio between running speed on the certain route and on well paved, horizontal and obstacle free road. The results suggested that the existing evacuation routes were not sufficient and that the direction of evacuation need adjustment. It was found that relatively slower runners that were in front of faster runners would potentially decrease the average evacuation speed. Vertical evacuation routes, such as along steep hills or high buildings, must be wide enough (to ensure a low crowd density) and easily accessible (to ensure a higher evacuation route speed) to avoid traffic jams. The number of people to be evacuated and road condition are vital factors to determine the evacuation routes to the selected shelters.

Keywords: *tsunami; evacuation; simulation; numerical; multi agent; Indonesia; running speed*

Vol. 34, No. 1, page 50 (2015)

1 INTRODUCTION

Tsunamis have been generated several times along the Sunda Trench, the boundary between the Indo-Australian and Eurasian plates to the south of Java Island. Fig. 1 presents five locations of earthquakes relatively near to the study area that triggered tsunamis over the last 155 years based on National Geophysical Data Center/World Data Service (NGDC/WDS) (2014). Damanik et al. (2010) determined that a seismic gap region almost due south of Parangtritis (Fig. 1), may experience earthquakes in the near future. Kongko (2012a) compiled the run-up data and indicated that the 2006 tsunami run-up at Parangtritis and the surrounding area ranged from 2.8 to 5.5 m.

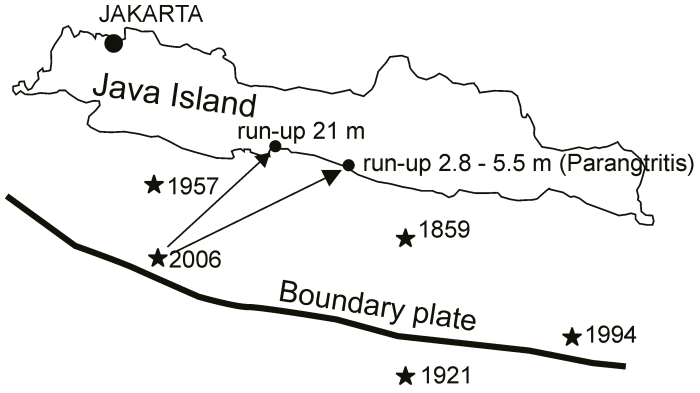

Figure 1. Tsunamigenic earthquakes over the last 155 years (based on NGDC/WDS, 2014)

Kongko (2012b) conducted a more detail numerical model using an M_w 8.2 earthquake with an epicenter located along the boundary between the Indo-Australian and Eurasian plates at approximately 210 km to the south of the beach. The maximum tsunami height at Parangtritis beach was 4.47 m where the tsunami travel time was 33 min. German Indonesian Tsunami Early Warning System (2010) recommended that when the tsunami height is greater than 3 m, the people at Parangtritis Beach should evacuate to Shelter 1, Shelter 2 and Shelter 3 (Fig. 2).

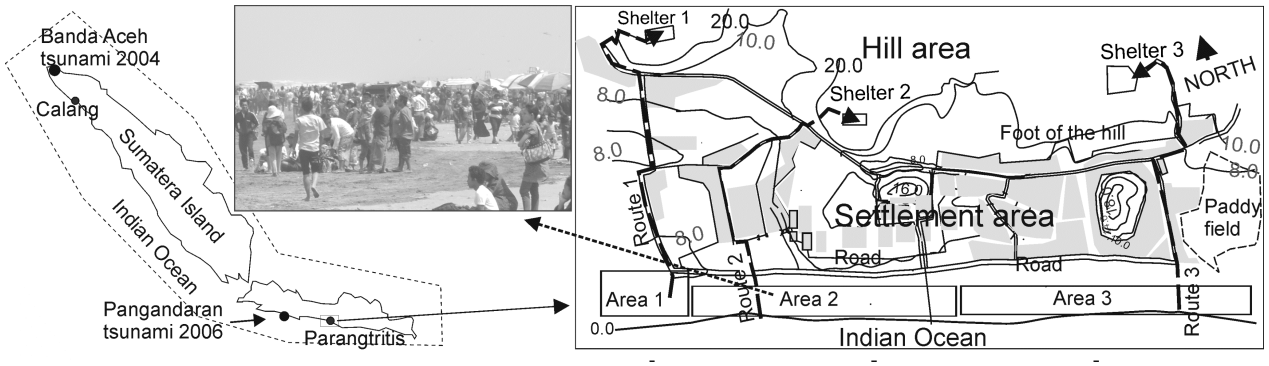

Figure 2. Map of Parangtritis Beach and the crowd during a public holiday.

Parangtritis is a local tourist destination located at the southern coast of Java Island in Indonesia, facing the plate boundary between the Indo-Australian plate and Eurasian plate. Fig. 2 presents the sketch of Parangtritis Beach and the crowd during a public holiday. The detail of the evacuation routes is given in Figure 7. With a nearly vertical hill behind the beach area, a tsunami of 10 m high may run up, be reflected by the hill, and inundate the entire area Triatmadja (2010). Thus, the hill would become the only safe evacuation area during a large scale tsunami event.

Routes to temporary safe grounds or shelter areas have been prepared at Parangtritis Beach. The final portions of the routes that lead to the hill's top are two narrow stairways to Shelter 1 and Shelter 2 and two paved 7- to 8-m-wide roads to Shelter 3 (Fig. 2). These facilities are expected to save a lot of lives during tsunami hazard and hence evaluation of the capacity and suitability of the evacuation routes should be conducted. One of the methods is using simulations of evacuation. Physical simulations of an evacuation require a significant number of people, resources and funding, good coordination, and preparation time. In contrast, mathematical simulations are considerably less expensive risk free and easier to manage, although they cannot provide evacuation experience and skills to residents. Affan et al. (2010) demonstrated that their mathematical simulation software, which accommodates user input on their preferred routes at Banda Aceh, helps them to justify their evacuation routes. In an area where most of the people are tourists, it is not possible or at least not efficient to educate and provide the experience necessary to tourists regarding evacuation because they only stay for a short duration. For such conditions, the mathematical simulation is a good alternative for evaluating the preparedness of the infrastructures. Many mathematical modeling approaches are available to simulate evacuations, as described by Hamacher and Tjandra (2001) and Gwynne et al. (1999). The spectrum of such mathematical models is broad, with macro- to micro-scale simulations. The latter is extremely detailed with regard to the dynamics of the evacuees and is suitable for the present study. Numerical simulations of an evacuation related to tsunami events have been conducted for a number of cases in Indonesia. Noda et al. (2010) simulated the evacuation of residents during a tsunami event in Meulaboh, Indonesia. The model was capable of simulating the evacuation process in large areas serviced by roads and junctions. Goto et al. (2012) performed another similar simulation with additional types of evacuees, namely, normal walkers, slow walkers, motorcyclists, and automobiles. They suggested that the use of automobiles should be limited, whereas the use of motorcycles to evacuate to certain shelters is necessary. Imamura et al. (2012) demonstrated that even after 45 min, only 37.7% of evacuees managed to escape from the hypothetical tsunami in Padang during the worst-case scenario.

The goal of this research is primarily to evaluate the performance of a relatively simple mathematical model based on the Dijkstra algorithm to evaluate a predefined evacuation routes, such as those in Parangtritis Beach, Indonesia.

2 MATHEMATICAL MODEL ALGORITHM

At the start of the evacuation simulation, all of the evacuees should have their own shortest paths as the primary routes that guide the evacuees toward a safe ground. Evacuees may divert slightly from the shortest path because of obstacles (or other evacuees). The most popular algorithm for determining the shortest path is most likely the A* (A star) algorithm developed by Hart et al. (1968). This algorithm is the core component of most animated games (Pinter 2001). Pinter (2001) improved the algorithm to provide smooth paths and turns. The smooth straight paths are achieved through an additional algorithm that checks whether the points along the line from the original position to the targeted position at typically 1/5 the size of the grid the unit overlap any neighboring blocked nodes. Such an improvement makes the algorithm requires additional computational resources. The Dijkstra algorithm Dijkstra (1959) is similar to the A* algorithm but without the heuristic feature (guessing the more likely shortest path to the target). In certain cases Dijkstra algorithm requires more computational time to check all nodes up to the target. However, when the shortest paths to the shelters from almost the entire nodes in the computational domain are required as in this study, Dijkstra algorithm is as good as A* algorithm and is easier to handle. Both algorithms are more suitable for defining the optimum evacuation routes rather than for simulating evacuations in which people must follow predefined routes. In this study, to be consistent with the goal of the research, it was assumed that the evacuees were obliged to go to a particular shelter based on their original location area along the beach. However, their shortest paths were determined based on Dijkstra algorithm. There were three evacuee areas, as shown in Fig. 2. The assumption appears reasonable when addressing the evacuation of people where most of the evacuees are visitors, such as at Parangtritis Beach. According to Badan Pusat Statistik Kabupaten Bantul (2013), the total number of residents in Parangtritis village was 7,653 people, and only 2,200 people lived in the Parangtritis Beach area. This was a small percentage when compared to the number of tourists during public holidays, which may surpass 20,000 people. These visitors are not familiar with the beach area and hence will largely follow the available evacuation route directions.

The simulation area was divided into square grids and nodes to identify the positions of the evacuees and obstacles in the entire simulation area. A number of models and software packages, such as EGRESS and FlightSim, use a similar technique (Hamacher, and Tjandra, 2001). Based on the average shoulder breadths of Indonesian residents, which are 41.7 and 38.2 cm for male and female adults, respectively (Laboratorium Perancangan Sistem Kerja dan Ergonomi-Teknik Industri -ITB, 2007), a uniform grid size (Δs) of 0.5 m × 0.5 m is selected, this approximately equals the area occupied by one person. The EXODUS software package typically uses the same grid size (Gwynne et al., 1999). In this study, Dijkstra algorithm was used to define the shortest paths of every node to the designated shelters. Along the selected shortest paths, the evacuees may change their directions to avoid the crowd by following the next best choice of paths based on the next smallest cost value of the surrounding nodes. At each node, the evacuees were given five best choices of movement.

3 RUNNING SPEED AND ASSUMPTIONS OF RUNNING BEHAVIOR AND CONSTRAINTS

Steudel-Numbers et al. (2009) argued that taller people run faster. They found that the male volunteers (179.6 cm), who were on average taller than the female volunteers (168.2 cm), ran most efficiently at 3.7 m/s, whereas the female volunteers ran at 2.9 m/s during a 5-min test run. The mean heights of male and female citizens of Indonesia are 158 and 147 cm, respectively (Frankenberg, et. al., 2003). Hence, the average Indonesian resident (healthy but not an athlete should be significantly slower. In fact, Imamura et al. (2012) simulated an evacuation during a tsunami event in Indonesia using a constant average running speed of 1.67 m/s, which was slightly faster than the preferred walking speed of 1.42 m/s (2006). Goto et al. (2012) used an even slower running speed of 1.5 m/s for average people when no other people were within 1 m^2. Several factors may affect the running speed of an individual: the (a) evacuee's physical condition (gender, age, health, disabilities), (b) preparedness (shoes, dress, any items or infant to carry), (c) distance of run, (d) crowd density, and the (e) road condition (soft sand, hard sand, paved road, steep slope, stairs, slippery road, stony road, road with obstacles, visibility).

The running speed as a function of age and gender may be determined based on the world running records. The following equation is set up to represent the impact of age and gender on running speed:

$$V_C = C\left(kA/A_0\right)^k e^{-(kA/A_0)}, \tag{1}$$

where V_c is the individual running speed capacity (running speed with no obstacles on a paved road) for a certain running distance. Both C and k are constants related to gender, age, and running distance. A is the age of the evacuee, and A_o is the optimum age for maximum running speed capacity. Based on Eq. (1), the maximum running speed capacity is $C\,k^k\,e^{-(k)}$ at $A = A_o$. The solid and dashed lines in Fig. 3 demonstrate that the equation is in good agreement with data for the best male and female athletes records based on Eisold (2003), IAAF (2012), and Mastersatheletics

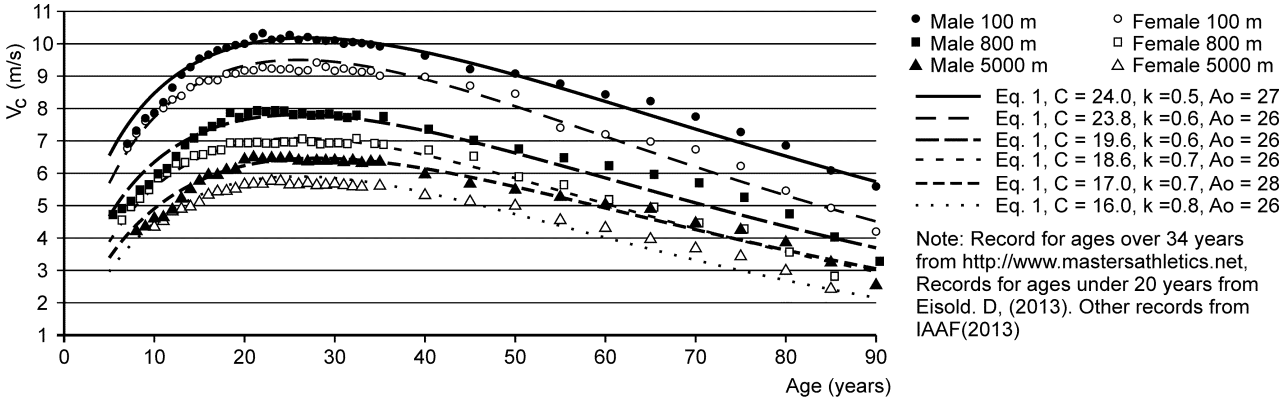

Figure 3. Best running speed capacities of male and female athletes versus age.

(2012) for appropriate *C, k*, and A_o values. Based on this equation, *C* is typically higher for males than females, whereas *k* exhibits the opposite trend. With a slightly higher value of *k*, the performances of female athletes tend to decline more rapidly with age. This conclusion is similar to that of Ransdell et al (2009). A_o is slightly higher for males for short-distance runs (100 m) and long-distance runs (5,000 m). The equation appears to fit the data relatively well until 80 and 90 years of age for females and males, respectively, after which it diverges significantly from the data. Assuming that the effect of age and gender on average people is somewhat similar to the best athletes, Eq. (1) may be expected to also fit average people, although with suitable C, *k*, and A_o values.

Fig. 3 also illustrates that the world running records drop significantly from distances of 100 to 800 m, after which it drops again, although only slightly, for even the 5,000 m distance record. People at Parangtritis Beach must run distances ranging from 500 to 1,500 m. Their running speed capacities during the evacuation based on the above discussion can be estimated based on a distance of 800 m. For a more realistic simulation of an evacuation, the running speed should be varied depending on the road condition by applying a speed factor *f* that represented the ratio between running speed on the certain roads and on well paved, horizontal and obstacle free road. When running closely with others, people may slow down slightly to avoid bumping into others. The inclusion of crowd density into the running speed equation is expected to simulate such behavior. Because discrete space is employed in the present algorithm, the crowd density is determined by the existence of evacuees at adjacent grid points either in front of or beside the evacuee of interest. Fig. 4 presents a possible situation surrounding an evacuee.

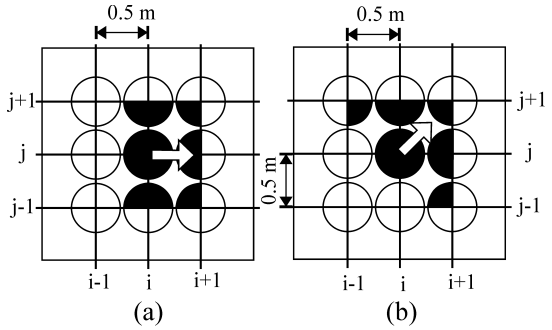

Figure 4. An evacuee at grid point (i,j) surrounded by eight evacuees at surrounding grid points. (a) Evacuee moving in the *X* direction and (b) evacuee moving 45° to the *X* direction.

Fig. 4 (a) illustrates evacuees moving to the right (east), and Fig. 4 (b) illustrates evacuees moving to the north east. The crowd density (*D*) for an evacuee at grid point (*i,j*) is assumed to follow Eq. (2):

$$D = \sum_{i=1}^{6} m, \qquad (2)$$

where m has a certain value at a grid point that is occupied by an evacuee; otherwise, $m = 0$. The maximum number of evacuees in Eq. 2 is six because the people behind the evacuee of interest are not considered, as in the case of Fig. 4. The values of m at one grid in front of or beside the grid point *(i,j)* is assumed to be 0.5 if the distance to the grid point (*i,j*) is Δs, $m = 0.25$ if the distance to the grid point (*i,j*) is $\Delta s\sqrt{2}$ and $m = 1$ at grid point *(i,j)*, as indicated by the percentage area that is filled with black in Fig. 4. Hence, based on Eq. (2), the values of D for an evacuee at grid point *(i,j)* are 3 and 2.75 for Fig. 4 (a) and Fig. 4 (b), respectively. The minimum value of D is 1, where there are no other people within 1 m^2 surrounding the evacuee of interest.

The running speed can then be calculated using Eq. (3):

$$V = C_D f V_C . \tag{3}$$

The value of f depends on the road condition, varying from nearly zero for very steep and narrow steps to 1.0 for well paved horizontal roads. The maximum value of C_D is unity, which is when nobody is around the evacuee. Assuming that C_D decreases exponentially with an increasing crowd density near the evacuee, C_D may be written as a function of D in Eq. (4) to yield the minimum value of $C_D = 0.2$. Goto et al. (2012) used a similar approach with a nonlinear function to represent the effect of the number of people per square meter on the running speed.

$$C_D = D^{-D/2} \tag{4}$$

The use of a square grid requires that the movement of the evacuee be conducted every Δl, which may equal either Δs or $\Delta s\sqrt{2}$, depending on the directions of the movement. The time step used in the simulation was 0.1 s to ensure that each evacuee travels a distance of less than Δs. This distance is stored and added up to the previous acquired distance. When the accumulated distance reaches Δl or greater, the evacuee may move to the adjacent node, and the residual distance is stored. However, if all the nodes of the best selection are occupied, the evacuee does not move, and the accumulated distance is void (Fig. 4b). This approach ensures that no evacuee jumps over another or simultaneously occupies the same node with another evacuee.

During one time step, the evacuees move in sequence until all of the evacuees obtain their opportunity. When an evacuee has completed the move for one time step or does not move because of a lack of acquired distance, the next evacuee gets a turn. This arrangement is realistic when everyone may run freely along the selected paths. However, in a crowded area, to make the movement realistic, the evacuees are assumed to be classified into five groups of different domination levels from 1 (most dominant) to 5 (inferior), which are assumed to depend on age. The most dominant evacuees are selected from those between 25 to 40 years of age for up to 20% of the total evacuees. When the number of evacuees within the specified range is not sufficient, additional evacuees of the maximum domination are selected from the population using a broader range of 20 to 50, 15 to 60, 10 to 70, and from less than 10 or higher than 70 years of age until the

required number is fulfilled. Subsequent levels of domination are then similarly assigned to evacuees starting from the age range from 25 to 40 years and following ranges until reaching 20% of the total number of evacuees. The selection method assumes that the number of evacuees at each level is the same. The group with the highest level of domination is given the first opportunity to move, followed by subsequent domination level groups. A similar variation of domination, but with additional complexities, is used by a number of professional software package to reflect the evacuee's attitudes during an evacuation (for example, by the Pathfinder software (Thunderhead Engineering, 2013). Kuligowski et al. (2010) reviewed 26 software packages dedicated to evacuation simulation in buildings, with 23 models including evacuee behavior.

4 PHYSICAL EXPERIMENTS

To determine an appropriate running speed of average people, experiments were carried out using a number of volunteers of different ages and gender. The experimental setting was as follows. First, the volunteers were asked to run a medium distance of 800 m as this represents the average distance of evacuation routes at Parangtritis Beach. The experiment was conducted at Universitas Gadjah Mada, where the volunteers ran 100 m back and forth eight times on flat paved ground. The health of each volunteer was not checked medically, but they declared that they were in good physical condition and capable of running. Therefore, the time of the experiment depended on the availability of the volunteers. When they were sufficiently rested, the volunteers had to run a short distance on the same paved ground and a type of stair to measure the effects on running speed. Another running experiment was carried out at Parangtritis Beach. The volunteers ran for a distance of 50 m on hard sand and another 50 m on soft sand. After sufficient rest, selected volunteers ran a complete path that was from the beach to the location of the safe ground. There were three complete paths, as given in Fig. 2 that represent possible running paths of the evacuees during a tsunami event. We returned to Parangtritis Beach once again to perform a test run for the last part of the evacuation route from the base of the hill to the safe ground. Only selected volunteers were tested. They had to run on a paved road of the same distance, and the results were used to calibrate *f* for the last part of the routes.

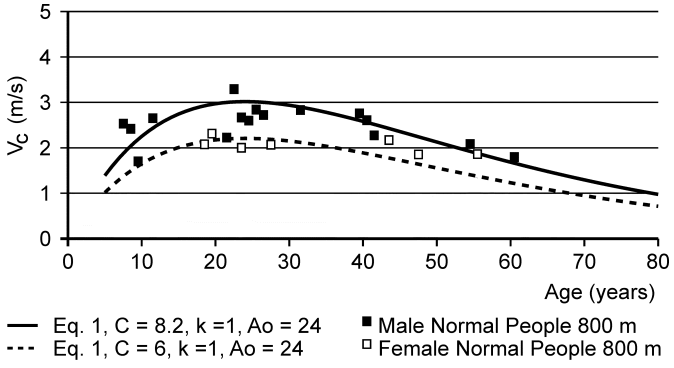

Figure 5. Running speed capacities of average Indonesian residents at 800 m distance.

Fig. 5 presents the results of the medium-running-distance tests on the paved road. In contrast to

Fig. 3, the data in Fig. 5 are more scattered along the line of Eq. (1) because the volunteers were selected randomly, whereas only the best were recorded in Fig. 3. C was expected to be significantly lower for average people than for the professional athletes. Fig. 5 indicates that Eq. (1), with $C = 8.2$, $k = 1$, and $A_o = 24$ for males and $C = 6$, $k = 1$, and $A_o = 24$ for females, may be used to represent the running speed capacities of average people. The simulation assumed that all of the evacuees follow the above coefficients.

The data of the running experiment are given in Table 1. The table illustrates that f equals 0.91 and 0.86 for hard sand and soft sand, respectively. For a mixture of steep and mild stairs leading to Shelter 2 (vertical to horizontal slopes of approximately 1:2 to 1:5) and mild stairs (average slope of 1:5) leading to Shelter 1 of Parangtritis Beach, the values of f were 0.19 and 0.27, respectively. The speed factor is significantly higher ($f = 0.40$ to 0.42) on a mildly sloping road (1:6 to 1:8), such as those leading to Shelter 3a at Parangtritis.

Table 1. Results of running experiment

Road condition	Number of Volunteers	Distance (m)	Average Speed (m/s)	Average Speed on Pave Road (m/s)	Speed factor
Hard Sand	15	50	5.26	5.76	0.91
Soft Sand	15	50	4.93	5.76	0.86
Stairs Route 1	2	220	1.38	5.20	0.27
Stairs Route 2	2	150	0.71	3.76	0.19
Steep Road Route 3	3	280	1.95	4.86	0.40
Complete path Route 1	3	1070	1.33	2.32	0.57
Complete path Route 2	3	850	1.81	2.68	0.67
Complete path Route 3	3	840	2.33	2.75	0.85

The running simulation along the complete paths of the evacuation routes at Parangtritis Beach was carried out using the same volunteers. Nine volunteers from 18 to 38 years of age were selected for the experiment. The average speed ratio may be deduced from the calibration results, which yield approximately 0.61, 0.80, and 0.80 for Routes 1, 2, and 3, respectively, whereas the experiment yielded average speed factors 0.57, 0.67, and 0.85, respectively (Table 1).

5 NUMERICAL MODEL PERFORMANCE

The model was tested using a number of male and female evacuees that were assumed to be normally distributed from 6 to 60 years of age with a mean and standard deviation equal to 30 and

12.5 years, respectively. The evacuees were placed randomly along narrow lanes of 3 m wide and 200 m long. The numbers of evacuees in the area were 150, 300, 600, 1,200, 1,800, and 2,400, yielding initial evacuee densities of 0.25, 0.5, 1, 2, 3, and 4 per square meter, respectively. Narrower crowd lanes of 1 m wide and 200 m long with the same initial numbers of evacuees per square meter as above were also tested for comparison. The evacuees had to reach a destination 700 m from the nearest evacuee or approximately 900 m from the furthest (Fig. 6).

A ratio (W) of the average running speeds to the average running speed capacities for a certain distance for all evacuees may be used as the evacuation route speed indicator measuring the effect of D and f on the running speed, as given in Eq. (5).

$$W = \sum_{i=1}^{n} \left(\frac{L_i / T_i}{V_{Ci}} \right), \tag{5}$$

where n is the number of evacuees, L_i is the running distance of evacuee i to the shelter, T_i is the time required by evacuee i to reach the shelter, and V_{ci} is the running speed capacity of evacuee i for a certain distance.

For the numerical performance test, the people were assumed to run at their running speed capacities ($f = 1$) for the 800 m distance but were dependent on the surrounding evacuees. Based on Eq. (1) with $C = 8.2$ for males and $C = 6$ for females and $k = 1$ and $A_o = 24$ for both males and females, the running speed capacities ranged from 1.6 to 3.02 m/s.

Each scenario was run five times, and the average results are given in Fig. 6. The variation of the results of each scenario was relatively small (less than 10% of the average, not shown in Fig. 6). The figure indicates that W increases as D decreases and becomes nears unity as D becomes approximately 1, where an evacuee may run freely without being affected by other evacuees. During the simulations, the lanes became wider as the faster runners tried to escape from the crowd. The lanes also became longer as the crowd dispersed because of running speed variations as well as the opportunity to run presenting itself. The 1 m lanes expanded up to approximately 6.5 times the initial width, whereas the 3-m-wide lanes expanded only up to 3.5 times. It took less than 5% of the total time of the evacuation for the crowd to expand completely during the test with the highest D value. This indicates that the effect of the initial D value is short lived. With a lower D value caused by a relatively more extensive lane expansion, the 1-m-wide lanes produce slightly higher values of W than the 3-m-wide lanes. The effect of age distribution is not significant on W for evacuees running in open spaces, as indicated by Fig. 6. The crowd of uniform age (30 years old) produces only slightly higher W, especially for low values of D. However, with even the same value of W, the total evacuation time of the uniform age crowd is reduced because the running capacity of the 30-year-old evacuees is higher.

To simulate the effect of fixed width lanes as if on a road with buildings as the boundaries, similar simulations of the above were carried out with walls along the boundaries of the lanes. With such

walls, the only way for the faster runners to run to the shelter is behind the slower runners while waiting for available space to overtake the slower runners so that they could run at their running capacities. The results demonstrated that the values of W are reduced significantly because of the wall boundaries (Fig. 6). For 1-m-wide lanes with wall boundaries, it becomes more difficult for the faster runners to overtake the slower runners as the availability of space becomes limited.

Based on Eq. (3), for $f = 1$ and assuming that all of the evacuees run at a uniform, constant speed, D and C_D are constant and equal to their initial value. In this case, W is equivalent to the initial C_D value, which is plotted in Fig. 6 as a dashed line. The figure indicates that all of the lanes without boundary walls resulted in higher values of W, indicated by the dashed line, because of the expansion and elongation of the crowd that led to lower crowd densities. The resulting W is close to the dashed line because the walls were included and because only elongation was possible. When D is relatively large, W becomes slightly higher than the dashed line as the elongation of the crowd becomes more significant. By using a normal age distribution, the blockages caused by slower runners produced significantly lower values of W, especially along narrow lanes. During the test condition for the 1-m-wide lane with boundary walls and normally distributed evacuee ages, slower runners in front slowed down the elongation of the crowd and resulted in an even lower value of W than the initial C_D value for a small D. At a large initial D, the elongation led to higher crowd density coefficients. The variation of W for each scenario may actually be larger than previously indicated for only five runs with random evacuee placements. This variation depends on whether the slower runners are in front of or behind the faster runners. Further experiments where the evacuees were arranged so that the faster runners were initially in front of the slower runners yielded significantly higher values of W, as shown in Fig. 6. Similarly, lower values of W were produced by arranging all of the faster runners behind the slower runners instead of placing them randomly. The difference between the results of placing the faster runners in front of and behind the slower runners indicates the approximate maximum variation due to random placement. Thus, the numerical model performs realistically.

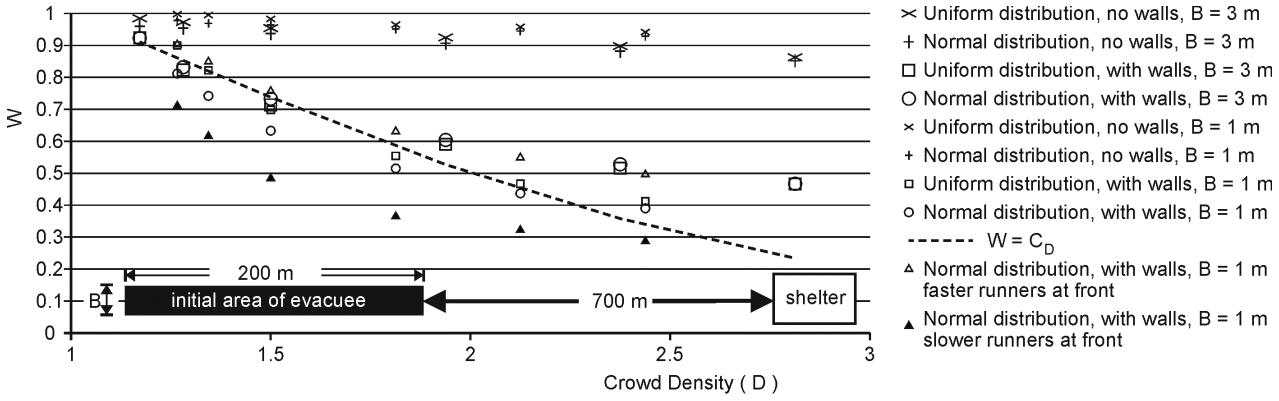

Figure 6. Effect of crowd densities and boundary walls on running speed.

6 SIMULATIONS OF AN EVACUATION AT PARANGTRITIS BEACH

The simulations were simplified by assuming that the people were ready to run after the shock. Such assumption represents the best situation for maximum survivals. In reality people may not evacuate immediately after the shock which may result in more casualties.

The beach area was divided into Areas 1, 2, and 3 with their respective evacuation routes, as depicted in Fig.7, to enable the investigation of W at each route for different crowd densities. First, the routes were tested using various numbers of evacuees without considering the effect of road conditions (f = 1) to evaluate the effect of D on W. The evacuees were assumed to be distributed randomly along the beach from the shoreline to approximately 50 m landward from the beach prior to evacuation (Fig. 7).

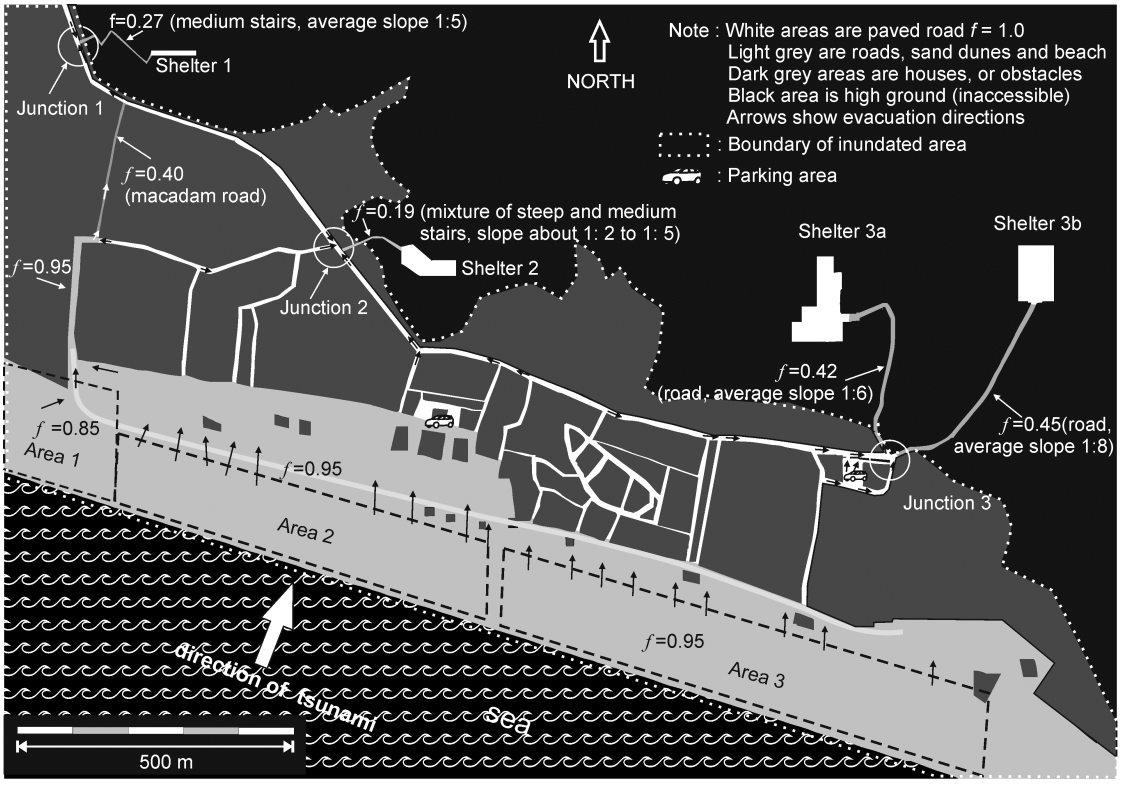

Figure 7. Parangtritis Beach and its evacuation routes

The simulations should be run many times with different positions of evacuees to observe the effect of random placement of evacuees. This would be very time consuming. Therefore, in addition to a simulation using random placement of evacuees, two extreme conditions were considered. These were placing faster runners in front of slower runners and vice versa as previously conducted during numerical performance tests. Such situations are very rare but may yield either the approximate maximum or minimum values of W or the number of survivals. The method may be considered as an alternative approach for statistical assessment of evacuation. The

results are shown in Fig. 8, where *W* decreases significantly with an increasing number of evacuees. The dashed lines represent the two extreme conditions. *W* decreases more rapidly along Route 2 compared to the other routes, suggesting the lower capacity of this route. Unlike Routes 1 and 2, which consist of narrow stairs at the end of the routes, Route 3 has four feeder routes and two main wide sloping roads leading to Shelters 3a which make the evacuation capacity considerably larger, as indicated by the significantly higher value of *W* in Fig. 8. No evacuation sign board is directed to this direction and hence Shelter 3b was not included in the simulation.

The inclusion of the speed factor *f* based on the road conditions into the simulation resulted in severe traffic jams, especially at Junction 2 of Route 2. The values of *W* decreased significantly for all of the routes, especially Route 2. When evacuating 2,000 people, the value of *W* for Route 2 was 0.25, indicating a highly inefficient evacuation route.

During special public holidays where 10,000 people were distributed evenly in Area 2 and 3 the values of *W* of Route 2 and 3 were reduced to 0.15 and 0.4 respectively (Fig.8b and 8c). This resulted in the survivals of merely 16% and 90% from Area 2 and Area 3 respectively after 33 minutes (Fig.9b and 9c). Figure 9 indicates that the percentage of survivals after 33 minutes were very low from Areas 1, and 2. In fact, Route 1 and Route 2 can accommodate only 800 people each, whilst Route 3 can accommodate up to 4500 people. These numbers of survivals were consistence for higher number of evacuee. With 2,000 evacuees in each Area, approximately 40% of the evacuees from Area 1 and 40% of evacuees from Area 2 survived. The survivals of Area 3 were slightly less than 50% when the number of visitors in that area was 10000 people. When the number of visitors at Area 2 is 5000 or more the traffic jam at Junction 2 was similar to that at Calang, Aceh in 2004.

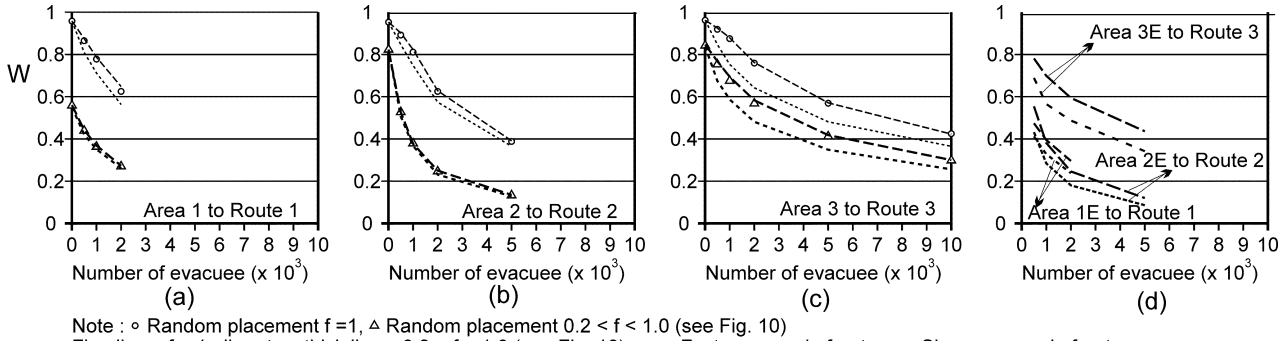

Figure 8. Performance of evacuation routes at Parangtritis Beach for various numbers of evacuees. (a), (b) and (c) evacuee from Area 1, 2 and 3 respectively. (d) evacuees from Area 1E,2E, 3E respectively.

Additional simulations were performed to observe the effect of the initial evacuees' positions. Areas 1, 2 and 3 were expanded to the north until the road along the base of the hill. These are referred to Areas 1E, 2E and 3E, respectively. The simulation indicated that *W* and the maximum

numbers of survivors of Areas 1E, 2E and 3E were only marginally higher than if the evacuees were contained in Area 1, 2 and 3 respectively (Fig. 9 and Fig. 10). However the effect of placing slower runners in front of the faster runners decreased the survival significantly for Area 1E and 2E. The spreading of the evacuees in larger area (Area 3E) increased the chance of survival. Apparently, the slower runners in the case of Area 1E and 2E arrived sooner at the stairs to the hill than the faster runners that were positioned far behind the slower runners and resulted in more blockage of the route.

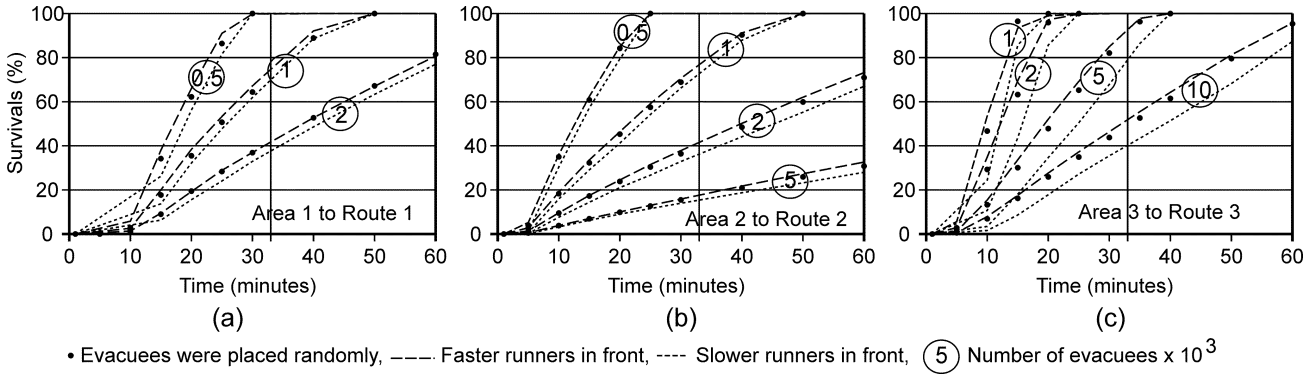

Figure 9. Survivals versus time (a) Evacuees from area 1 to Shelter 1 (b) Evacuees from Area 2 to Shelter 2 and (c) Evacuees from Area 3 to Shelter 3

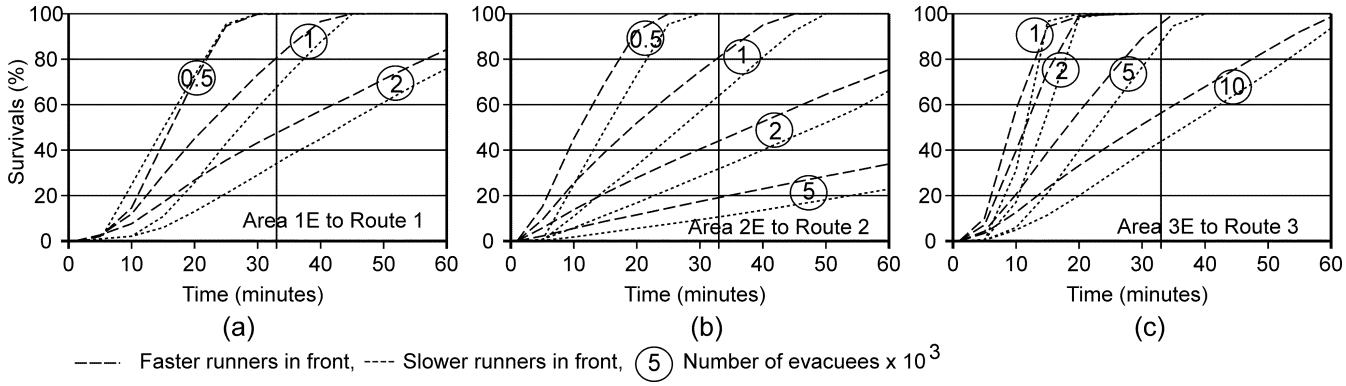

Figure 10. Survivals versus time (a) Evacuees from area 1E to Shelter 1 (b) Evacuees from Area 2E to Shelter 2 and (c) Evacuees from Area 3E to Shelter 3

The distance between Junctions 2 and 3 is approximately 1,150 m, or approximately 7 to 10 min travel time of evacuee. To decrease the severity of the jam at Junction 2, directing the evacuees at all of the junctions between Junctions 2 and 3 to Shelters 3a along the main road is worth considering. With this scenario, an evacuation simulation with 2,000 people in Area 2 and 2,000 people in Area 3 was conducted. After 33 minutes 78% (3174 people) and 22% (826 people) survived at Shelter 3 and Shelter 2 respectively. Comparing to Fig. 9(b), the result indicated an increase survival rate of 60% (corresponding to 1200 survivors) from Area 2. However, when 2,000 people were in Area 2 and 4,000 people were in Area 3, the total survivals were 5522 people

in which 874 people were at Shelter 2 and 4648 people were at Shelter 3. Therefore directing the evacuees between Junctions 2 and 3 to Shelters 3 along the main road should be conducted when the people in Area 3 is less than 4000. This suggests that the number of evacuees should be considered when determining evacuation routes. Redirecting evacuees from Junction 2 to Shelter 1 should not be considered even though Junction 2 is closer to Shelter 1 than to Shelter 3 because the capacity of Route 1 is limited.

The use of cars and motorcycles for the evacuation was not considered in this paper. However, as the main roads connecting Junctions 1, 2, and 3 were relatively dense with people during the simulations with 5,000 people or more, the use of cars could endanger the evacuees and even cause traffic jams that hinder evacuation. In addition, Junction 2 was completely packed with people after approximately 7 min, and thus, no cars or even motorcycles could pass through. Furthermore, when the evacuees at all of the junctions between Junctions 2 and 3 were directed to Shelter 3, the main road from Junction 2 to Shelter 3 became more crowded, which might block the cars and motorcycles that move in the opposite direction. The best way for buses, cars, and motorcycles to evacuate is to Shelter 3b. However, their effort to escape from the parking area to Junction 3 may hinder the evacuation because the routes to the main road and along the main road to Junction 3 were crowded during the evacuation.

7 CONCLUSION

A numerical model based on Dijkstra algorithm performs realistically and was successfully applied in simulating the evacuation of people through several routes during a tsunami event at a large beach area, where the running speed of the evacuees varied based on age, gender, crowd density, and road condition. An evacuation route speed indicator (W) may be used to measure the effectiveness of the route for different scenarios of evacuation. Placing the slower runners in front of the faster runners significantly reduced the value of W and the number of survivors. This result indicates that during an evacuation, people should run at their running capacity to decrease the total number of casualties. It also suggests that confused people or people who run slowly in front of others because of a number of reasons, such as looking for family members while running, helping slower runners, and bringing possessions, may hinder other evacuees and thus result in a reduced total number of survivals. Placing the slower runners in front of the faster runners or vice versa may be used to approximate the worst or the best possible evacuation scenarios respectively. The method may reduce the number of simulation runs.

The simulations showed that evacuation routes should be determined based on the number of evacuees as demonstrated by the simulation that during a crowded public holiday, the evacuees that arrived at all of the junctions between Junctions 2 and 3 should be directed to Shelters 3a to decrease the number of casualties. The evacuation routes of Parangtritis beach area should be improved especially Route 1 and Route 2.

ACKNOWLEDGMENT

The author would like to thanks the Directorate of Research and Public Service, the Directorate General of Higher Education, Ministry of National Education and Culture of Indonesia for the funding of this research. Thanks and appreciations are extended to all of the volunteers from the Tsunami Research Group Universitas Gadjah Mada for making the physical experiment possible. The author is also in debt to the reviewers of this paper.

REFERENCES

Affan. M., Goto. Y., and Agussabti (2010). "Tsunami Evacuation Simulation for Disaster Awareness Education and Mitigation Planning of Banda Aceh." *Proceedings 15 WCEE*, Lisboa

Badan Pusat Statistik Kabupaten Bantul (2013), *Bantul Dalam Angka 2013*, Bantul, Yogyakarta

Browning, R. C., Baker, E. A., Herron, J. A., Kram, R. (2006). "Effects of obesity and sex on the energetic cost and preferred speed of walking." *Journal of Applied Physiology,* 100(2), 390-398.

Damanik. R., Andriansyah., Putra. H.E., Zen. M.T. (2010), "Variations of b-values in the Indian Ocean – Australian Plate Subduction in South Java Sea." *Proceedings of The Bali 2010 International Geosciences Conference and Exposition,* Bali

Dijkstra. E.W., (1959), A Note on Two Problems in Connexion With Graphs, Numerische Mathematik 1, 269-271

Eisold, D., (2013). "The best performances by 5- to 19-year-old athletes from 47 countries." *International Age Records*, < http://age-records.125mb.com/>(March 5, 2013).

Frankenberg, E., Jones, N., R. (2003). "Self-Rated Health and Mortality: Does the Relationship Extend to a Low Income Setting?." On-Line Working Paper Series, California Center for Population Research, UC Los Angeles.

German Indonesian Tsunami Early Warning System. (2010), "Peta Rencana Evauasi Tsunami Kabupaten Bantul, D.I. Yogyakarta", *Tsunami Kit*<http://www.gitews.org/tsunami-kit/id/E4/sumber_lainnya/rencana_evakuasi/jawa_bantul/Peta%20Evakuasi%20Kabupaten%20Bantul.jpg> (February25 ,2014)

Goto, Y., Affan.M., Agussabti. Y., Nurdin., Diyah. K. Yuliana., and Ardiansyah. (2012). "Tsunami Evacuation Simulation for Disaster Education and City Planning." *Journal of Disaster Research* 7(1), 92-101.

Gwynne, S., Galea, E.R., Owen. M., Lawrence, P. J., and Filippidis, L. (1999). "A Review of the Methodologies Used in Evacuation Modelling." *Fire and Material,* 23(6), 383-388

Hamacher, H. W., and Tjandra, S. A. (2001). *Mathematical Modeling of Evacuation Problems: a State Of* The *Art*, Rep. No. 24 (2001), Fraunhofer-Institut für Techno- und Wirtschaftsmathematik, Fraunhofer.

Hart, P.E., Nilsson, N. J., Raphael, H. (1968). "A Formal Basis for the Heuristic Determination of Minimum Cost Paths." *IEEE Transaction of System Science and Cybernetics*, 4(2), 100-107.

Imamura, F., Muhari, A., Mas, E., Pradono, M. H., Post, J., Sugimoto, M. (2012). "Tsunami Disaster Mitigation by Integrating Comprehensive Countermeasures in Padang City, Indonesia." *Journal of Disaster Research.*, 7(1), 48-64.

International Associations of Athletes Federations (IAAF), (2012). "All Time Best, Men and Women." *Records and Lists* < http://www.iaaf.org/ > (May 01, 2013)

Kongko, W. (2012a). *South Java Tsunami Model Using Resolved Data Tsunamigenic Sources,* Doctoral Dissertation at Franzius Institut, Leibniz Universitaet Hannover Germany, Franzius-Institut für Wasserbau und Küsteningenieurwesen, Mitteilungen Heft 99

Kongko, W. (2012b)."Gempa-Tsunami di Selatan Jawa: Potensi, Simulasi Model, dan Upaya Mitigasinya." Presented at *Seminar Memperingati Gempa Yogyakarta,* Kabupaten Bantul DIY, 26 Mei 2012

Kuligowski, E.D., Peacock.R.D., and Hoskins. B. L. (2010), *A Review of Building Evacuation Models,* 2nd Edition, Technical Note 1680, NIST, US

Laboratorium Perancangan Sistem Kerja dan Ergonomi-Teknik Industri -ITB, (2007). "Lihat Data" *Data* Antropometri *Indonesia*, < http://antropometri.ti.itb.ac.id/lihat_data.php> (April 23, 2013)

Mastersatheletics. (2012), "All Time World Ranking." *Track and Field-World Records***,** **<**http://www.mastersathletics.net/index.php?id=3>(Nov. 18, 2012)

National Geophysical Data Center / World Data Service (NGDC/WDS): *Global Historical Tsunami Database*. National Geophysical Data Center, NOAA. doi:10.7289/V5PN93H7 (Feb. 12, 2014)

Newcomb, K., R and McCann, W. R. (1987). "Seismic History and Seismotectonic of the Sunda Arc." *Journal of Geophysical Research*, Vol. 92, No. B1,

Noda, I., Soeda, S., Yamashita, T., Nurdin, Y., Yuliana, D.K. (2010). "Disaster Evacuation Simulation with Multi-Agent System Approach using NetMAS for Contingency Planning (Meulaboh case study)." *Proc., 5th Ann. Int. Workshop & Expo on Sumatra Tsunami Disaster & Recovery*., TDMRC, B. Aceh, Indonesia, 76-79.

Pinter, M. (2001), Toward More Realistic Pathfinding, Features, < http://www.gamasutra.com/view/feature/131505/toward_more_realistic_pathfinding.php> , (April 2014)

Ransdell, L. B., Vener, J., Huberty, J. (2009). "Masters Athletes: An Analysis Of Running, Swimming And Cycling Performance By Age And Gender." *J. Exercise Science and Fitness,* 7(2), S61–S73.

Steudel-Numbers, K.L., Wall-Scheffler, C.M. (2009). **"**Optimal running speed and the evolution of hominin hunting strategies**."** *Journal of Human Evolution.,* 56(4), 355 – 360.

Thunderhead Engineering. (2013), *Pathfinder Technical Reference.,* Manhattan, USA

Triatmadja, R. (2010). *Tsunami: Kejadian, Penjalaran, Daya Rusak dan Mitigasinya,* Gadjah Mada University Press.

Wilkinson, F. (2005). "Coastal Design and Tsunami Mitigation for Shelter/House Reconstruction on The West Coast Aceh." *Int. Symposium Disaster Reduction on Coasts Scientific-Sustainable-Holistic-Accessible,* Monash University, Melbourne, Australia.

ISSN 8755-6839

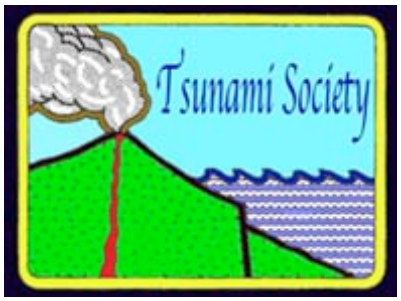

SCIENCE OF **TSUNAMI HAZARDS**

Journal of Tsunami Society International

Volume 34 **Number 1** **2015**

TSUNAMI SOCIETY INTERNATIONAL, 1741 Ala Moana Blvd. #70, Honolulu, HI 96815, USA.

WWW.TSUNAMISOCIETY.ORG